



Experimental study of intruder components in light neutron-rich nuclei via single-nucleon transfer reaction

Wei Liu¹ · Jian-Ling Lou¹ · Yan-Lin Ye¹ · Dan-Yang Pang²

Received: 15 December 2019 / Revised: 9 January 2020 / Accepted: 11 January 2020 / Published online: 6 February 2020
© China Science Publishing & Media Ltd. (Science Press), Shanghai Institute of Applied Physics, the Chinese Academy of Sciences, Chinese Nuclear Society and Springer Nature Singapore Pte Ltd. 2020

Abstract With the development of radioactive beam facilities, studies concerning the shell evolution of unstable nuclei have recently gained prominence. Intruder components, particularly *s*-wave intrusion, in the low-lying states of light neutron-rich nuclei near $N = 8$ are of importance in the study of shell evolution. The use of single-nucleon transfer reactions in inverse kinematics has been a sensitive tool that can be used to quantitatively investigate the single-particle orbital component of selectively populated states. The spin-parity, spectroscopic factor (or single-particle strength), and effective single-particle energy can all be extracted from such reactions. These observables are often useful to explain the nature of shell evolution, and to constrain, check, and test the parameters used in nuclear structure models. In this article, the experimental studies of the intruder components in low-lying states of neutron-rich nuclei of He, Li, Be, B, and C isotopes using various single-nucleon transfer reactions are reviewed. The focus is laid on the precise determination of the intruder *s*-wave strength in low-lying states.

Keywords Single-nucleon transfer reaction · Intruder component · Light neutron-rich nuclei

1 Introduction

Electrons that are confined within atoms by the Coulomb potential have a well-known shell structure. Shell-like phenomena also appear in finite nuclear systems. Almost 70 years ago, Mayer and Jensen developed a theoretical model to describe the nuclear shell structure [1, 2], which was formed by placing the single nucleon (proton or neutron) in a mean field created by all other nucleons. According to the well-established mean-field theory, nucleons fill in the single-particle orbitals in shells that are characterized by the conventional magic numbers: 2, 8, 20, 50, 82, and 126. However, for nuclei far from the β -stability line, especially those in the light mass regions where the concept of a mean field is less robust, exotic rearrangements of the single-particle configuration often occur and may result in the inversion of some orbitals or the emergence of various intruder components [3], leading to the disappearance of the traditional magic numbers and the appearance of new magic numbers [4]. This rearrangement may also result in shifts in the single-particle energies (or orbitals), essentially affecting all the features of the nuclear structure and leading to processes such as deformation [4, 5]. The strongly attractive interaction between neutrons and protons has been considered as the main cause of this rearrangement of orbitals in exotic nuclei [4]. The evolution of the shell structure in unstable nuclei, including the rearrangement of orbitals, intrusion, and shifts in the single-particle energies, can now be partly described in terms of a new mean-field model wherein the monopole effect of

This work was supported by the National Key R&D program of China (No. 2018YFA0404403), and National Natural Science Foundation of China (Nos. 11775004, U1867214, and 11535004).

✉ Jian-Ling Lou
jllou@pku.edu.cn

¹ School of Physics and State Key Laboratory of Nuclear Physics and Technology, Peking University, Beijing 100871, China

² School of Physics, Beijing Key Laboratory of Advanced Nuclear Materials and Physics, Beihang University, Beijing 100191, China

the tensor force [5–7] and three-body forces [8] are implemented.

It has been found that the energy gap between the $1d_{5/2}$ and $2s_{1/2}$ shells changes significantly for light neutron-rich nuclei near $N = 8$, leading to the appearance of some s -wave components in low-lying states. These two orbitals can even be inverted, meaning that the $2s_{1/2}$ orbital can intrude into $1d_{5/2}$, and occasionally even into $1p_{1/2}$ [9, 10]. One widely noted example is the ground state of the one-neutron halo nucleus of ^{11}Be , which possesses an unusual spin-parity of $1/2^+$ that is dominated ($\sim 71\%$) by an intruder $2s_{1/2}$ neutron coupled to the inert core of $^{10}\text{Be}(0^+)$ [11, 12]. The intrusion of the s -wave into the ground state of ^{11}Be is clearly responsible for the formation of its novel halo structure. Intruder s -wave components have also been observed in the low-lying states of the nuclei such as ^9He , $^{10,11}\text{Li}$, $^{12,13,14}\text{Be}$, $^{13,14}\text{B}$, and $^{15,16}\text{C}$, and have been widely studied in various experiments using different methods in order to understand their exotic structure [13]. The transfer reaction is one of the most common experimental methods used to study the intruder components in the wave functions of exotic nuclei.

The transfer reaction, especially the single-nucleon transfer reaction, is a sensitive experimental tool used to selectively populate certain interesting states in nuclei. These populated states can be described using either the original or a residual nucleus as a core with the transferred nucleon in an orbital around it. The spin-parity of the selectively populated state can be assigned because the oscillation behavior of differential cross sections (DCSs) depends on the transferred angular momentum l [14, 15]. The contribution of the transferred nucleon to each populated state is usually described by the spectroscopic factor (SF), which is often extracted by comparing the experimental with the theoretical DCSs. It has been disputed for several years whether SF is useful for experimental observation. Can SF be directly connected to nuclear structure? Several experiments have been performed in order to address these questions. The conclusion that has been reached is that the relative or normalized SF is related to the occupancy or vacancy number of a certain orbital [11, 16], rather than the SF that is directly extracted (reaction model dependent). If both the SF and the excitation energy for each populated state with the same orbital j are known, the effective single-particle energy of the orbital j can also be determined [14, 15]. Therefore, transfer reaction is a quantitative tool that can be used to probe the intensity of the single-particle orbital component (or occupancy/vacancy number), the spin-parity of the populated state, and the effective single-particle energy of a nuclei that is at a distance from the β -stability line.

Unlike stable nuclei, the half-lives of radioactive beams are relatively short; hence, single-nucleon transfer reactions have to be performed in inverse kinematics. The missing mass method, in which only the energies and angles of the recoil light particles are measured, is a commonly used method for investigating transfer reactions in inverse kinematics. This experimental method has some advantages over normal kinematic measurements. However, in this regard, a number of experimental challenges are generated, such as the precise detection of charged particles with low energies. Several new experimental techniques have therefore been developed to overcome these issues, and several new detection arrays have been constructed in various laboratories. In this paper, the basic modules and the advantages and disadvantages of the typical experimental setups are introduced in detail. The studies concerning the single-particle orbital intruder components in light neutron-rich nuclei are also reviewed.

This paper is organized as follows: the basic concepts of transfer reaction are outlined in Sect. 2; the advantages and disadvantages of normal and inverse kinematics are analyzed, and the missing mass method is introduced in Sect. 3; some typical experimental setups for the single-nucleon transfer reactions used worldwide are summarized in Sect. 4; studies that have been conducted using single-nucleon transfer reactions to investigate the exotic nuclear structure of neutron-rich He, Li, Be, B, and C isotopes are reviewed in Sect. 5; and a brief summary is given in the final section.

2 What can we learn from the transfer reaction?

2.1 What is a transfer reaction?

Generally, a transfer reaction can be written as



where A and a are the target and the projectile nuclei, and B and b represent the residual and the outgoing particles, respectively. This means that when projectile a collides with target A , a nucleon (proton or neutron) or a cluster (such as ^4He) is transferred to form a new final system that comprises b and B . A stripping reaction describes the situation in which the nucleon or cluster is transferred from projectile a to target A , and a pick-up reaction describes the situation when the nucleon or cluster is transferred to projectile a . If only one nucleon is transferred, the result is known as a single-nucleon transfer reaction. Figure 1 shows the different kinds of single-nucleon transfer reactions when ^{11}Be collides with a proton or deuteron target. When a deuteron beam impinges on a ^{11}Be target, the one-

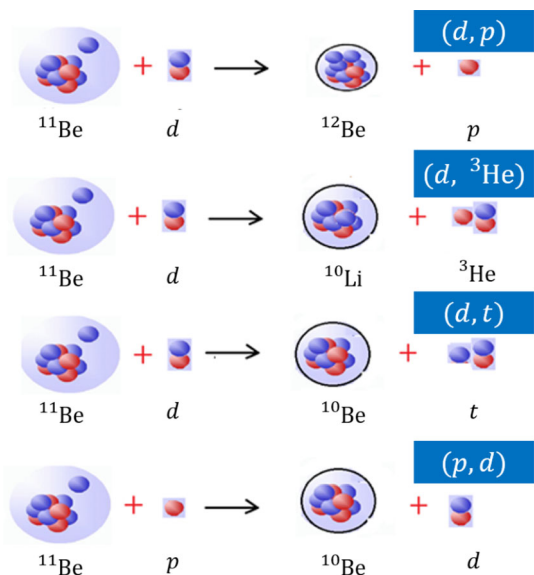


Fig. 1 (Color online) Single-nucleon transfer reactions induced by ^{11}Be impinging on the proton or the deuteron target

neutron and one-proton transfer reactions are written as $^{11}\text{Be}(d, p)^{12}\text{Be}$ (or $^{11}\text{Be}(d, t)^{10}\text{Be}$) and $^{11}\text{Be}(d, ^3\text{He})^{10}\text{Li}$, respectively. If a ^{11}Be incidence occurs, the experiment has to be performed in inverse kinematics, and the corresponding expressions are changed to $d(^{11}\text{Be}, p)^{12}\text{Be}$ (or $d(^{11}\text{Be}, t)^{10}\text{Be}$) and $d(^{11}\text{Be}, ^3\text{He})^{10}\text{Li}$. The recoil charged-particle proton (or triton) and ^3He are measured in both cases. Both the $d(^{11}\text{Be}, t)^{10}\text{Be}$ and $d(^{11}\text{Be}, ^3\text{He})^{10}\text{Li}$ reactions are typical stripping or nucleon-removing reactions in inverse kinematics, while the $d(^{11}\text{Be}, p)^{12}\text{Be}$ reaction is a pick-up or nucleon-adding reaction. The single-particle knockout reaction is another typical nucleon-removing reaction, but will not be reviewed in this paper.

2.2 Angular distributions and spin-parity

The DCS of $A(a, b)B$ to a given final state in B oscillates as a function of the scattering angle. The structure of the oscillation (that is, the positions of the maxima and minima) depends on the transferred angular momentum l . This behavior can be understood via the simple momentum diagram shown in Fig. 2. If we assume that the incident projectile has a momentum \vec{p} and the momentum that is transferred to the target nucleus is \vec{p}_t , only a small reduction is observed in the magnitude of the momentum of a beam particle for a small scattering angle θ , as seen in the vector diagram (Fig. 2), which is built according to the conservation of momentum. From the cosine rule, we have:

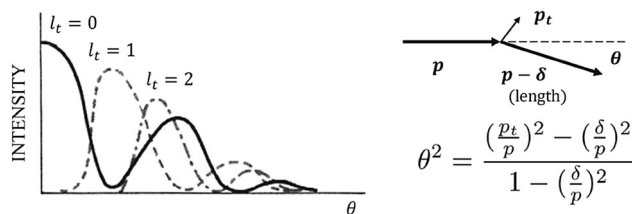


Fig. 2 On the left side of the diagram, DCS is given as a function of the scattering angle θ in the laboratory frame for the different transferred orbital angular momentum l . The vector diagram on the right explains the relationship between θ and the transferred angular momentum l . This figure is from [17]

$$\cos\theta = \frac{p^2 + (p - \delta)^2 - p_t^2}{2p(p - \delta)}. \tag{2}$$

If we make use of the second order expansion, which is referred to as

$$\cos\theta \approx 1 - \frac{\theta^2}{2}, \tag{3}$$

then we have,

$$\theta^2 = \frac{\left(\frac{p_t}{p}\right)^2 - \left(\frac{\delta}{p}\right)^2}{1 - \left(\frac{\delta}{p}\right)^2}. \tag{4}$$

The reduction δ in the length of the vector p is small in comparison to the length of the actual transferred momentum p_t , meaning that the term δ/p can be dropped [17]. The expression θ^2 can therefore be simplified to

$$\theta^2 \approx \left(\frac{p_t}{p}\right)^2. \tag{5}$$

In the classical picture of a transfer reaction, the nucleon is usually transferred at the surface of the target nucleus, and the angular momentum \vec{L} is given by [17]

$$\vec{L} = \vec{p}_t \times \vec{R}, \tag{6}$$

where \vec{R} is the vector radius of the target nucleus. From quantum mechanics [15], we have

$$L^2 | \phi \rangle = l(l + 1)\hbar^2 | \phi \rangle. \tag{7}$$

It is therefore easy to deduce that:

$$\theta_0 \approx \frac{p_t}{p} = \frac{\sqrt{l(l + 1)}\hbar}{pR}, \tag{8}$$

where θ_0 is the angle of the first maxima in the cross section. This indicates that θ_0 is different for each different transferred momentum l , and that θ_0 increases with l . This trend can be seen in Fig. 2. The transferred orbital angular momentum l , and therefore the parity of the populated states, can be assigned in conjunction with other

experimental information or shell model predictions. Transfer reactions can also be used to assign the total angular momentum j of the selectively populated states [14].

Using the reaction $^{14}\text{B}(d, p)$ as an example, Fig. 3 depicts the angular distributions for this reaction in the $3/2^-$ ground state (solid curve), the $5/2^-$ (dashed curve), and the $7/2^-$ (dotted curve) excited states of ^{15}B . The DCSs in Fig. 3 were calculated using FRESKO [18] with global optical potentials obtained from Daehnick [19], and Koning and Delaroche [20] for the entrance and exit channels, respectively. It is evident that the oscillation behavior of the angular distributions depends largely on the transferred angular momentum l .

2.3 Spectroscopic factor

The single-nucleon transfer reaction is a powerful experimental tool that can be used to study the structure of certain selectively populated states. The contribution of the transferred nucleon to each populated state is usually described by SF, which is often determined by comparing the DCSs that are deduced from experiment with those obtained from theoretical calculation. The functional expression is as follows:

$$\left(\frac{d\sigma}{d\Omega}\right)_{\text{exp}} = C^2 \text{SF}_{\text{exp}} \left(\frac{d\sigma}{d\Omega}\right)_{\text{theo}}, \quad (9)$$

where C^2 is the isospin Clebsch–Gordan coefficient, which is sometimes omitted. The value for this amounts to 1.0 for the (d, p) transfer reaction [14]. $\left(\frac{d\sigma}{d\Omega}\right)_{\text{exp}}$ and $\left(\frac{d\sigma}{d\Omega}\right)_{\text{theo}}$ are the DCSs extracted from experiments and various reaction models, respectively. It should be noted that the expressions $\left(\frac{d\sigma}{d\Omega}\right)_{\text{theo}}$ are often different when sourced from

different reaction codes. For example, the code FRESKO [18] and DWUCK [21], gives

$$\left(\frac{d\sigma}{d\Omega}\right)_{\text{theo}} = \left(\frac{d\sigma}{d\Omega}\right)_{\text{FRESKO}} = \frac{2J_f + 1}{2J_i + 1} \left(\frac{d\sigma}{d\Omega}\right)_{\text{DWUCK}}, \quad (10)$$

where J_i and J_f describe the spin of the initial and final nuclei.

The distorted wave born approximation (DWBA) is the most common approximation theory that is used to calculate the transfer reaction DCSs $\left(\frac{d\sigma}{d\Omega}\right)_{\text{theo}}$. For a given reaction, the theoretical DCS is given by

$$\left(\frac{d\sigma_{\beta\alpha}}{d\Omega}\right)_{\text{theo}} = \frac{\mu_\alpha \mu_\beta}{(2\pi\hbar^2)^2} \frac{\kappa_\beta}{\kappa_\alpha} |T_{\beta\alpha}(\kappa_\beta, \kappa_\alpha)|^2, \quad (11)$$

where μ_α (κ_α) and μ_β (κ_β) are the reduced masses (wave numbers) in the entrance and exit channels, respectively, and $T_{\beta\alpha}$ is the transition amplitude. This equation takes the distortion of the incoming and outgoing waves caused by the nuclear potential U between the projectile and the target at the entrance ($a + A$, α) and exit partitions ($b + B$, β) into account. Assuming that the transfer reaction occurs in one step (first-order DWA or DWBA), the transition amplitude $T_{\beta\alpha}$ can be written [15]

$$T_{\beta\alpha} = \int \chi^{(-)}(k_\beta, r) \langle \Phi_\beta | \Delta U | \Phi_\alpha \rangle \chi^{(+)}(k_\alpha, r) dr, \quad (12)$$

where r is the relative distance between the projectile and the target ($r_{\alpha(\beta)}$ in the entrance (exit) channel), and $\chi^{(+)}(k_\alpha, r)$ is the “distorted” wave composed of an incoming plane wave in the α state and the outgoing scattered waves. Similarly, $\chi^{(-)}(k_\beta, r)$ is the outgoing distorted wave in the channel β . The waves $\chi^{(-)}(k_\beta, r)$ and $\chi^{(+)}(k_\alpha, r)$ are obtained by solving the Schrodinger equation using an assumed potential for the outgoing and incoming channels, respectively. The potentials are usually extracted from the elastic scattering DCSs using the optical model (OM). The extracted potentials are known as optical model potentials (OPs).

In the case of reactions on unstable nuclei, the elastic scattering data is not always available, resulting in larger uncertainties in the DWBA calculations. Moreover, as deuteron is relatively loosely bound (only 2.22 MeV), it is easy to break up in the presence of a target nucleus. This breakup channel can couple with the transfer channel, affecting the SF_{exp} , of which the accurate extraction is important. To account for this mechanism, Johnson and Soper [22] devised the adiabatic wave approximation (ADWA), which uses nucleonic potentials and explicitly includes deuteron breakup. An extension of this method was developed by Johnson and Tandy [23] to include the finite range effects (FR). As stated in [11], the SFs extracted using the adiabatic model (FR-ADWA) are

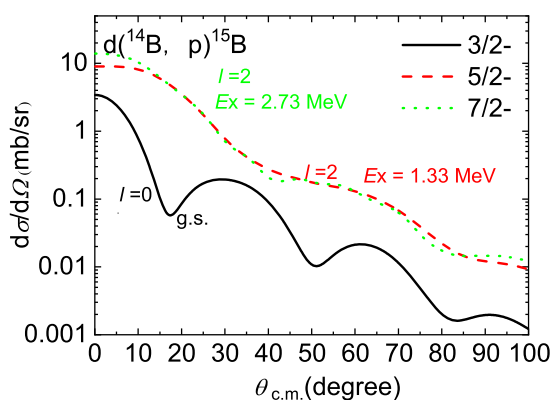


Fig. 3 (Color online) Angular distributions of the $^{14}\text{B}(d, p)$ transfer reaction to the $3/2^-$ ground state (solid curve), the $5/2^-$ (dashed curve), and the $7/2^-$ (dotted curve) excited states in ^{15}B , produced using a radioactive ^{14}B beam at 25 MeV/nucleon. The curves were calculated using FRESKO [18] and systematic optical potentials

“stable” across measurements at four energies for the (d, p) reactions, and are insensitive to the applied OPs, demonstrating the advantages of using this method as compared with extraction using the normal DWBA approach. This is why the FR-ADWA model is generally adopted for analysis of the transfer reaction. It is worth noting that these four measurements are performed under almost identical experimental conditions using the same set of OP parameters [11].

The SF that is extracted experimentally is sensitive to the choice of OP applied and also to several other practical experimental conditions [11, 16]. It has therefore been widely disputed whether it is a good experimental observable. Conceptually, SF is used to describe the occupancy of a valence nucleon at a single-particle orbit in a mean field created by other nucleons. For example, for an orbit with spin j , the total degeneracy number produced by the independent-particle model (IPM) should be $2j + 1$. In the case of configuration mixing based on the shell model approach, this number may be split into several states which are composed of the same j -wave with specific intensities. Shell model calculations that use appropriate effective interactions and model spaces could, in principle, predict the SF of a particular wave (single-particle orbit) in an energy eigenstate. However, the experimentally observed SFs are often smaller than those predicted by shell models, an effect that is exhibited as a reduction or quenching factor. This quenching phenomenon was firmly established via $(e, e'p)$ knockout reactions [24, 25]. This quenching effect is also generally confirmed in nuclear reactions such as single-particle knockout or transfer reactions. Using these reactions, the SF_{exp} can be extracted by comparing the experimentally measured cross section with that calculated assuming a pure single-particle state [26, 27] [Eq.(9)]. As an individual SF_{exp} can be sensitive to the choice of OPs and the practical experimental conditions (as aforementioned), the sum rule method was developed to define the relative SF and the general quenching factor [28]. The quenching factor in the nucleon transfer reaction is defined as

$$F_q = \frac{1}{2j + 1} \left[\sum \left(\frac{\sigma_{\text{exp}}}{\sigma_{\text{theo}}} \right)_j^{\text{rem}} + \sum \left(\frac{\sigma_{\text{exp}}}{\sigma_{\text{theo}}} \right)_j^{\text{add}} \right], \quad (13)$$

where the sum of adding and removing the relative cross sections for a given l, j represents the total degeneracy (sum rule) of that orbit [16].

It is challenging to measure the nucleon-removing and nucleon-adding reactions that take place in radioactive beams using the same experiment because of the limited beam intensity. If the nucleon-adding or nucleon-removing data were available for a given nucleus, the function for the quenching factor requires that the total strength adds up to

the number of vacancies in the closed shell, or the number of particles outside it [16], and the quenching factor is therefore modified to

$$F_q = \frac{1}{2j + 1} \left[\sum \left(\frac{\sigma_{\text{exp}}}{\sigma_{\text{theo}}} \right)_j \right]. \quad (14)$$

For example, a consistent quenching factor of approximately 0.55 for a large number of nuclei, with a root-of-mean-square spread of 0.10 was reported in [16]. Once the sum rule is established, the individual SF_{exp} can be normalized through the sum rule to give the intensity (percentage) of the wave component. This normalized SF is much less sensitive to the OP, or other parameters that are used and can therefore be reasonably utilized for comparison with the theoretical predictions. In other words, even for the same reaction, it is hard to directly compare the experimental SFs extracted from different measurements and analyzed using various sets of OP options without any normalization procedure [16]. Only the intensities (percentages) or the normalized SF (also called relative SF in some studies) can be directly compared, unlike the directly extracted experimental SFs of the wave components.

It is worth noting that the SF normalization procedure does not change the ratio between the SF_{exp} of different populated states in the final nucleus with the same spin-parity. Hence, the ratio, which is equivalent to the SF normalization, is often used in experiments [3, 29].

2.4 Effective single-particle energy

The IPM assumes that nucleons lie on single-particle energy orbits with no correlation between them. The single-particle energy of a particular orbit/state, which is equal to the energy needed for one nucleon to be excited from the ground state to this orbit/state, can therefore be measured simply. The shell model is based on a mean-field theory, in which the correlations between nucleons (protons and neutrons) are taken into consideration [15]. In this case, the single-particle (uncorrelated) energies are not directly observed, as real nuclei are correlated systems by nature. However, they can be obtained from experimental data using the normalized SF and the excitation energy of each populated state according to the sum rule [28].

Based on the Macfarlane–French sum rule [28], for the nucleon-removing reaction of a given nucleus A , the number of nucleons populated in a shell j (occupancy number) of A , $G^-(j)$, is

$$G^-(j) = \sum_k (SF)_k. \quad (15)$$

For the neutron-adding reaction of a nucleus A , the number of holes in a shell j (vacancy number) of A , $G^+(j)$, is

$$G^+(j) = \sum_k \frac{(2J_f + 1)_k}{2J_i + 1} (\text{SF})_k, \quad (16)$$

where J_i and J_f is the spin of the initial and final state (k), respectively. It should be noted that Eqs. (15) and (16) are simple equations used for a spin zero target such as deuteron. This sum rule has been tested in neutron transfer reactions carried out by Schiffer et al. [25]. The neutron-adding, neutron-removal, and proton-adding transfer reactions of the four stable even Ni isotopes were measured in the study, with particular attention paid to the cross section determinations. It was found that the valence-orbit occupancies extracted from the sum rule are consistent with the changing number of valence neutrons, as are the vacancies for protons, both at the $<5\%$ [25] level. This sum rule has also been used in the reactions of $d(^{13}\text{B}, p)$ [30], $d(^{19}\text{O}, p)$ [31], and $d(^{12}\text{B}, ^3\text{He})$ [32], among others.

If the excitation energies and spectroscopic strengths, referred to as the normalized or relative SFs, respectively, for all the relevant states with the same transferred angular momentum l are available, the effective single-particle energies (ESPE) can be given by the centroid [15]:

$$\varepsilon(j) = \frac{\sum_k G^+(E_k^+ - E_0) + G^-(E_0 - E_k^+)}{G^+ + G^-}, \quad (17)$$

where the sum covers all of the final excited states k , $\varepsilon(j)$ is the ESPE, and E_k^\pm is the excitation energy for the state k in nucleus $A \pm 1$. E_0 is the energy at the ground state of nucleus A . For reactions in which nucleons are added, such as (d, p), we have

$$\varepsilon(j) = \frac{\sum_k \frac{(2J_f + 1)_k}{(2J_i + 1)} (\text{SF})_k E_k}{G^+(j)}, \quad (18)$$

where SF_k is the relative or normalized SF for the state k . This can be simplified to

$$\varepsilon(j) = \frac{\sum_k (2J_f + 1)_k (\text{SF})_k E_k}{\sum_k (2J_f + 1)_k (\text{SF})_k}. \quad (19)$$

This formulation was presented in [30], and is equivalent to that given in [33].

For example, the calculation of ESPE using Eq. (19) for the reaction $d(^{13}\text{B}, p)$ to the low-lying states in ^{14}B is as follows. The populated low-lying states in ^{14}B were constructed via the coupling of one sd -shell neutron to the $3/2^-$ ground state of ^{13}B . This coupling leads to a $(1, 2)^-$ doublet for $1\pi(1p_{3/2})^- 1\nu(2s_{1/2})$, and $(1, 2, 3, 4)^-$ and $(0, 1, 2, 3)^-$ multiplets when the transferred neutron populates the $1d_{5/2}$ and $1d_{3/2}$ orbitals, respectively. Configuration mixing between states with the same spin and parity in ^{14}B is possible, especially for the neutron $2s_{1/2}$ and $1d_{5/2}$ orbitals because of the smaller energy gap between these two orbitals. Figure 4 shows the angular distributions of

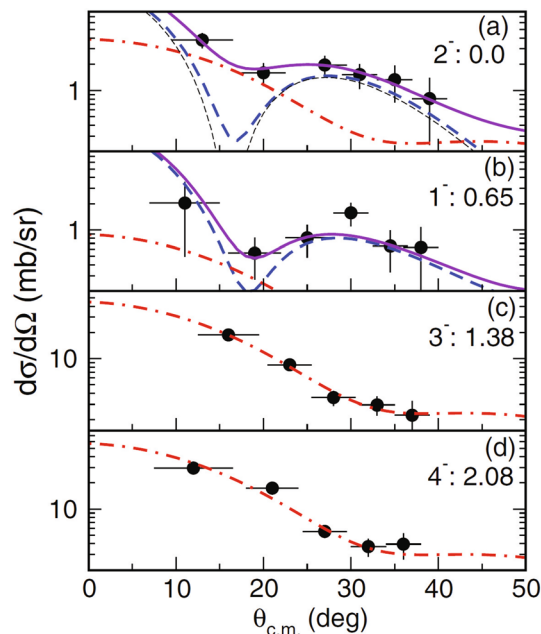


Fig. 4 (Color online) The DCSs for the $^{13}\text{B}(d, p)$ reaction to different excited states in ^{14}B . The horizontal bars represent the angular range of each data point, while the vertical bars stand for the statistical error. The thick-dashed, dot-dashed, and solid curves correspond to the DWBA calculations with $l = 0, 2$, and $0 + 2$, respectively. The thin-dashed curve in **a** shows the $l = 0$ result for the 2_1^- state before averaging over the scattering angle. This figure is from [30]

the $d(^{13}\text{B}, p)$ reaction to four low-lying states in ^{14}B . Only the 2_1^- , 1_1^- , 3_1^- , and 4_1^- states were populated; therefore, only the SFs for these four states could be extracted from this experiment. In Fig. 4a and b, it was found that it is difficult to fit the 2_1^- and 1_1^- DCSs using only the s -wave ($l = 0$) components (blue thick-dashed curves). However, when a little d -wave component was taken into consideration, the fitting of the angular distributions can be improved, indicating that these two states are made up of a mixture of s - and d -waves. If the effect of the $1d_{3/2}$ orbital is ignored, the spectroscopic strengths or the normalized SFs for the unobserved 2_2^- and 1_2^- states can be deduced using the assumption that the pairs of 2^- and 1^- levels are formed by orthogonal combinations of the $2s_{1/2}$ and $1d_{5/2}$ configurations. According to the orthogonal rule, the wave functions for these two states are written as

$$\begin{aligned} |J_1^- \rangle &= \alpha_J v(2s_{1/2}) + \beta_J v(1d_{5/2}), \\ |J_2^- \rangle &= -\beta_J v(2s_{1/2}) + \alpha_J v(1d_{5/2}), \end{aligned} \quad (20)$$

where $J = 1$ and 2 , $\alpha_J \times \alpha_J = \text{SF}(l = 0)$ and $\beta_J \times \beta_J = \text{SF}(l = 2)$ for the 2_1^- (or 1_1^-) state, and $\beta_J \times \beta_J = \text{SF}(l = 0)$ and $\alpha_J \times \alpha_J = \text{SF}(l = 2)$ for the 2_2^- (or 1_2^-) state. Based on the results of experimental observation of the 2_1^- and 1_1^- states, the s -wave (d -wave) SFs are determined as

0.17(5)(4) (0.71(5)(20)) and ≤ 0.06 (0.94(20)(20)) for the unobserved 2^- and 1^- states, respectively. This simple orthogonal method has been widely used in experiments, such as $d(^{15}\text{C}, p)$ [29], and $d(^{11}\text{Be}, p)$ [3].

The excitation energies (E_x) and SFs for each of the populated states are listed in Table 1 [30]. Using Eq. (16), the holes are determined to be 1.9 ± 0.2 and 5.9 ± 0.3 for the $2s_{1/2}$ and $1d_{5/2}$ orbitals, respectively. These two values are in close proximity to the 2.0 and 6.0 predicted by IPM. The ESPE for the $2s_{1/2}$ and $1d_{5/2}$ orbitals are calculated at approximately 0.5 ± 0.1 and 2.0 ± 0.4 MeV, respectively, using Eq. (17). These results demonstrate that the s orbital is lower than the d orbital in ^{14}B , which is different from the orbital arrangement described by the conventional shell model but is similar to other $N = 9$ isotones ^{13}Be and ^{15}C .

3 Experimental methods

3.1 Normal kinematics

One of the most effective ways to measure the (d, p) , $(d, t)m$, and $(d, ^3\text{He})$ reactions when using a beam of deuteron and a stable target is with a high-resolution magnetic spectrometer in order to record the recoil charged particles p , t , and ^3He that are emitted from the reactions. The high precision and low background noise are two typical advantages of normal kinematics. The typical energy resolution of the excited states in a final nucleus reaches approximately several tens of keV. For example, the Q -value spectrum for the $^{13}\text{C}(d, p)^{14}\text{C}$ reaction with a deuteron beam at 17.7 MeV in normal kinematics is shown in Fig. 5 [34]. Three closely spaced excited states can clearly be identified at $E_x = 6.73, 6.90,$ and 7.34 MeV in

Table 1 The excitation energies and normalized SFs for the low-lying states in ^{14}B [30]

Spin-parity	$E_x(\text{MeV})$	SF($l = 0$)	SF($l = 2$)
2^-	0	0.71(5)(20)	0.17(5)(14)
1^-	0.654	0.94(20)(20)	≤ 0.06
3^-	1.38		$\equiv 1.0$
2^-	1.86	[0.17(5)(4)]	[0.71(5)(20)]
4^-	2.08		1.0
(1^-)	4.5	≤ 0.06	[0.94(20)(20)]
Eq. (16)		1.9 ± 0.2	5.9 ± 0.3

The SFs are normalized to $\text{SF}(3^-) = 1.0$ and the uncertainties are (fit)(theory). The SFs in the middle brackets are calculated from experimental observation, assuming that the pairs in the 2^- and the 1^- levels are formed via the orthogonal combination of the $2s_{1/2}$ and the $1d_{5/2}$ configurations

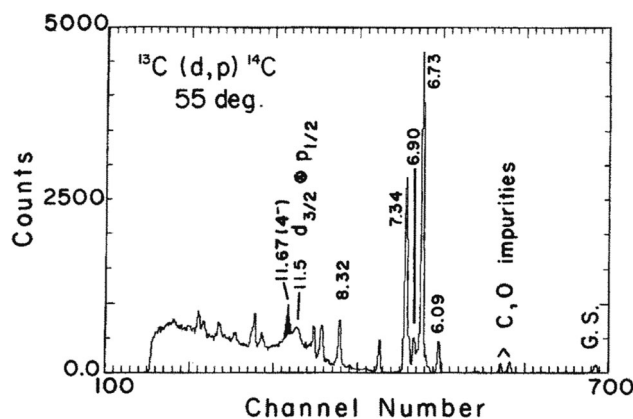


Fig. 5 The Q -value spectrum for $^{13}\text{C}(d, p)^{14}\text{C}$ with a 17.7 MeV deuteron beam using normal kinematics [34]

^{14}C , with an average resolution of approximately 60 keV [34].

3.2 Inverse kinematics

It is challenging to use normal kinematics with radioactive beams that have relatively short half-lives and low separation energies, because it is nearly impossible to use them as targets. Inverse kinematics is usually applied in such cases wherein the deuteron or the proton is used as target and the radioactive beam is used as the projectile.

The vector diagram for the reaction $A(a, b)B$ in inverse kinematics is shown in Fig. 6. The center of mass (CM) vector v_{cm} has the same direction as the projectile, with the length

$$v_{\text{cm}} = \frac{m_a}{m_a + m_A} \times v_a^{\text{lab}}, \tag{21}$$

where m_a (v_a^{lab}) and m_A are the mass (velocity) of the projectile and target, respectively. The vector diagram in Fig. 6a illustrates the case of (a) $d(A, t)B$, $d(A, ^3\text{He})B$, or $p(A, d)B$. After the reaction takes place, the heavy particle is moving forward with little change in either velocity or direction. According to the conservation of momentum and energy, it is easy to obtain a rough estimate of the vector length of the light (heavy) particle in the CM frame, labeled v_{cm}^l (v_{cm}^h) in Fig. 6a. For example, the mass of the outgoing light particle d is nearly two times that of the target p in the reaction $p(A, d)B$; however, the momentum that this particle carries in the CM frame is approximately equal to the whole of the CM momentum. The vector v_{cm}^l is therefore nearly half the length of v_{cm} . The precise value depends upon the reaction Q -value; however, the basic form of the vector diagram is always the same as that seen in Fig. 6a. As a result, the light reaction products are emitted in a forward direction, focusing onto a cone of angles at around 40° relative to the direction of the beam.

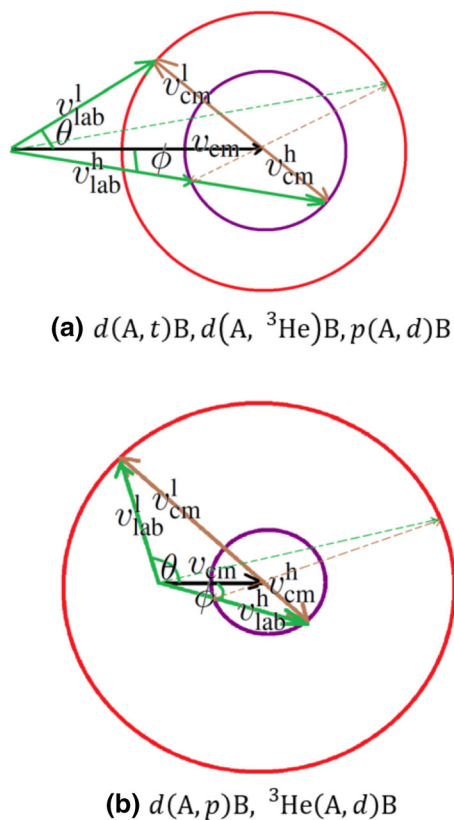


Fig. 6 (Color online) Vector diagrams for the reactions of **a** $d(A, t)B$, $d(A, {}^3\text{He})B$, $p(A, d)B$; and **b** $d(A, p)B$ and ${}^3\text{He}(A, d)B$, in inverse kinematics. The large and small circles represent the possible vector scope of the light and heavy particles in the CM frame, respectively. The thick solid and thin-dashed lines denote the low- and high-energy branches, respectively

There are two energy solutions for each angle followed by the outgoing light particles, referred to as the low-energy and high-energy branches, which are shown as the thick solid and thin-dashed lines, respectively, in Fig. 6a. The low-energy branch (solid curves) of these light particles corresponds to the high-energy branch of the heavy particles and to the smaller CM angles of heavy particles, and hence (typically) to the branch with higher DCSs [17]. However, it should be noted that the energy of the light particles in this branch is extremely low, which leads to numerous difficulties in accurate measurement.

In the reaction $d(A, p)B$ (or ${}^3\text{He}(A, d)B$), the outgoing light reaction products are lighter than the target, which implies that their CM velocities v_{cm}^{l} are greater than v_{cm} and the vector diagram is remarkably different from that in case (a) [see Fig. 6b]. It is evident that the light particles can be emitted backwards, reaching a maximum angle of 180° in the laboratory frame. Similar to case (a), there are two branches. The energy of the light particles, corresponding to the branch with the higher cross section, is still

extremely low. Therefore, there are significant challenges associated with detecting these particles.

The kinematics of the different reaction channels induced when a radioactive beam of ${}^{14}\text{B}$ at 20 MeV/nucleon collides with a deuteron target is shown in Fig. 7. The energies of the outgoing light particles are given as a function of their angles in the laboratory frame, corresponding to the part with the high cross section. The dotted, dash-dotted, dashed, and solid curves describe the reactions of $d({}^{14}\text{B}, {}^3\text{He})$, $d({}^{14}\text{B}, t)$, $d({}^{14}\text{B}, d)$, and $d({}^{14}\text{B}, p)$, respectively. The maximum energy of the light particles for each reaction channel is illustrated using the arrowed line, which corresponds to a CM angle of 20° . It is evident that the energies of ${}^3\text{He}$, t , d , and p are less than 3.1, 2.0, 1.9, and 6.5 MeV/nucleon, respectively, which are particularly low. These particles have had to force their way through the target before being detected, and have lost energy during this process. Considering the relatively lower beam intensity and smaller DCSs of the transfer reaction (at one or two magnitudes of order lower than elastic scattering), it is therefore better to use a thick target in order to obtain sufficient statistics concerning the angular distribution. However, because of the energy loss of the light particles within the target and the measurement of light particles, a thin target should be used for the accurate detection of light particles in order to obtain a Q -value spectrum with better resolution. The thickness of the target should therefore be determined especially for each particular experiment in inverse kinematics. When plastic CH_2 or deuterated polyethylene CD_2 is used, a typical thickness between several hundreds of $\mu\text{g}/\text{cm}^2$ and several mg/cm^2 is required. A more detailed account in this regard is given in [14].

It is worth noting that the angular scope of the light particles produced from different reaction channels is highly different. If the solid angles of the detectors are near

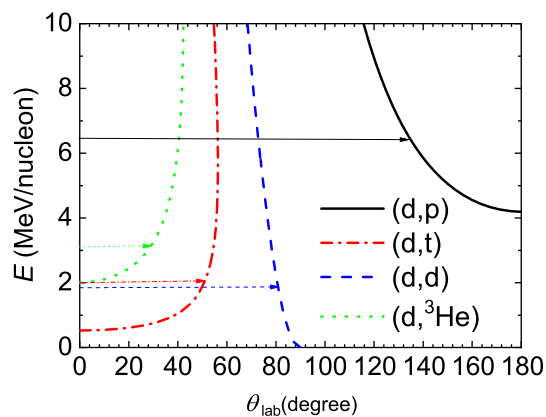


Fig. 7 (Color online) Kinematics of the different reaction channels induced using a radioactive beam of ${}^{14}\text{B}$ at 20 MeV/nucleon on a deuteron target. The arrowed lines point out the energies of the light particles (low-energy branch) at a CM angle of 20°

4π , several reaction channels can be measured in one experiment. For a (d, p) reaction in inverse kinematics, the light particles are emitted backwards in the laboratory frame, with the highest cross sections. Protons are almost the only possible products at backward angles; hence, particle identification (PID) is relatively easy. In a (d, t) or a $(d, {}^3\text{He})$ reaction, the recoil of t or ${}^3\text{He}$ moves in a forward direction, where several particles from other reaction channels are found, which indicates that accurate PID is more important as well as difficult. In this case, the measurements of the coincidence between the light particles and the residual nuclei are often required.

3.3 Missing mass method

For the transfer reaction $A(a, b)B$ in inverse kinematics, the whole CM angular range of the residual particles B can be covered in a small range in laboratory frame. A 4π coverage of a reaction is therefore easily achieved by placing detectors that cover only a small range around the direction of the beam. However, because of the inadequate range covered by laboratory systems, the energy and angle resolution required for this kind of measurement are too high to be achieved in most cases. An alternative solution is to simply identify the residual b particles, without measuring the residual B nuclei in the forward angle. The energies and angles of the light b particles are therefore usually measured, and the excitation energy (or Q -value) spectrum of the heavy B particles is then reconstructed using the following function [15].

$$Q = \left(\frac{m_a}{m_B} - 1\right) \times E_a + \left(\frac{m_b}{m_B} + 1\right) \times E_b - \frac{2(m_a m_b E_a E_b)^{1/2} \cos\theta}{m_B}, \tag{22}$$

where m_a (E_a), m_b (E_b), and m_B are the mass (energy) of projectile a , outgoing light particle b , and heavy particle B , respectively. θ is the outgoing angle of b relative to the direction of the beam in the laboratory frame. Although the nucleus of the B under investigation is not measured, all bound and unbound states can be derived using Eq.(22). The technique of reconstructing the Q -value spectrum or the excitation energy spectrum (E_x) of one of two ejectiles without actual measurement is called the missing mass (MM) method. One of the few techniques that can be used for the spectroscopic study of unbound states [15], the MM technique is also the most commonly used to investigate the single-nucleon transfer reaction using a radioactive beam in inverse kinematics. The precise measurement of the light particles, including their energies and angles, is the most important aim when the MM method is adopted for use in experimentation.

Typical Q -value spectra that have been reconstructed from the energies and angles of the recoil light particles using the MM method are shown in Fig. 8. The spectra were simulated using the Geant4 package [35], taking into consideration the beam profile (double Gaussian distributions in a circle with a radius of 10 mm), the dispersion of the radioactive beam (2%), the thickness of the target, the energy threshold (1 MeV), the energy (1%), the angular resolution of the light-particle detectors, and the energy loss, both in the target and the dead layer of the light-particle detectors. The simulation describes the reaction of $d({}^{14}\text{B}, p)$ to the ground state, the first ($E_x = 1.33$ MeV), and the second ($E_x = 2.73$ MeV) excited states in ${}^{15}\text{B}$ with a radioactive beam of ${}^{14}\text{B}$ at 20 MeV/nucleon. The typical resolution is less than 1 MeV (FWHM) when the target thickness and angular resolution are 3.0 mg/cm^2 and 1.8° , respectively. The result is shown in the upper picture of Fig. 8, where three bound excited states can clearly be discriminated in ${}^{15}\text{B}$. This means that if the energies and the angles of the recoil protons are measured, the resolution of the Q -value spectrum is adequate for the identification of different low-lying excited states in ${}^{15}\text{B}$. If the target thickness is increased to 3.6 mg/cm^2 and the angular resolution is changed to 1.5° , the corresponding Q -value spectrum is as seen in the lower image of Fig. 8. Although the resolution is worse than that of the upper image, the three peaks can still be clearly identified. This means that if the target thickness is increased, the Q -value resolution

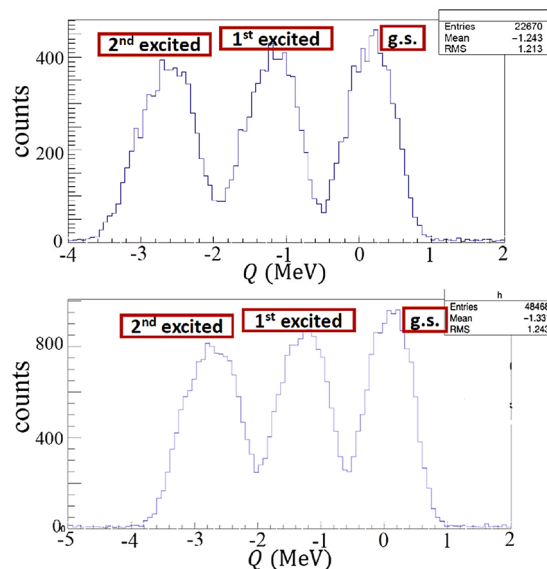


Fig. 8 The Q -value spectra, which were simulated using the Geant4 package [35] for $d({}^{14}\text{B}, p)$ to the ground state, the first ($E_x = 1.33$ MeV), and the second ($E_x = 2.73$ MeV) excited states in ${}^{15}\text{B}$ at 20 MeV/nucleon. The CD_2 target thickness (angular resolution) is 3.0 and 3.6 mg/cm^2 (1.8° and 1.5°) for the upper and lower spectrum, respectively

worsens, which can be compensated for by improving the angular resolution.

In more complicated cases where the excitation energies of several states in an unmeasured nucleus are closer to each other, it is hard to discriminate these states by merely using the MM method. Several methods are often applied to solve this problem, the simplest of which is to decrease the target thickness to several hundred or tens of $\mu\text{g}/\text{cm}^2$. However, new problems concerning statistics are generally created if this simple method is used because of the limitations to the intensity of the radioactive beam and the relatively small cross sections of the transfer reactions. Another method is to maintain (or increase) the target thickness while adding new high-resolution detectors such as γ -ray detectors. It is worth noting that the efficiency of γ -rays is usually extremely low, and the coincidence efficiency of the γ -rays and recoil light particles should therefore be carefully considered. The most advanced method used is the active-target time project chamber (AT-TPC) detector. These are discussed in detail in Sect. 4.

4 Typical experimental setup

As aforementioned, it is most important that the recoil light particles are precisely measured if a high-resolution excitation energy (or Q -value) spectrum for the unmeasured nucleus B is to be obtained. Several different detection arrays have been constructed for this purpose. In this section, the detector setups that are frequently used in different radioactive beam facilities around world for single-nucleon transfer reactions in reverse kinematics are introduced.

4.1 Silicon detector arrays and γ detector arrays

The energy and angle of the emitting light particles are often measured using silicon detector arrays. The first layer of a detector array that is constructed using highly segmented silicon detectors is generally known as a ΔE detector, through which light particles can force their way while losing a specific amount of energy. The second or the third layer that is used to stop the light particles is called the E detector. Large area silicon detectors or CsI(Tl) crystals are usually used. Particle identification (PID) is achieved from the amount of energy lost in the ΔE and E detector, while positional or angular information is provided by the segmented silicon detector. The energy of the emitted particles is often too low to penetrate the ΔE detector. In this case, the time of flight (TOF) and ΔE method is applied to identify the recoil light particles, as in [3].

Several silicon detector arrays have been constructed over the past three decades, such as MUST2 [36] and TIARA [37] at GANIL. MUST2 is a telescope array that was designed for the detection of light charged particles that are produced via direct reactions using exotic ion beams, with an active area of 10 cm by 10 cm in each module. A typical module is composed of the first stage of a double-sided silicon strip detector with 128 strips on each side, followed by a second stage of 4.5 mm-thick Si (Li) segmented with 2 pads of 2×4 , and finally a 3 cm-thick CsI segmented into 4×4 pads. The structure of one module is presented in Fig. 9.

The MUST2 array has undergone significant extension over the past few years and now comprises 10 modules, providing a large angular coverage with an efficiency of approximately 70% at angles of up to 45° [36] by reasonable placement. The combination of the hundreds of μm -thick silicon detectors and the several cm-thick CsI allows measurement over a large energy range, while simultaneously measuring both time and position. The reconstruction of the TOF, momentum, total kinetic energy, and trajectory is therefore possible, and the construction of the MM spectrum is achievable using this array. Several experiments have been performed using the MUST2 array, exploring dozens of radioactive isotopes, such as ^9He [39], ^{10}He [40], ^{13}O [41], ^{21}O [42], and ^{61}Fe [43].

In order to cover a large range of angles, a well-organized, quasi- 4π position sensitive silicon array, TIARA, was developed at GANIL. The ultimate goal of TIARA is to perform direct nuclear reaction studies in inverse kinematics with radioactive ion beams. This array is comprised of a set of single-layer silicon detectors. The main part consists of an octagonal barrel that is formed from 8 resistive charge division detectors with a pair of large annular double-sided silicon strip detectors (SiHyBall) covering each end of the barrel (Fig. 10). Because the target is almost totally covered with silicon detectors, unique target changing mechanisms and electronics and data acquisition systems had to be developed. Detailed information can be obtained in [37].

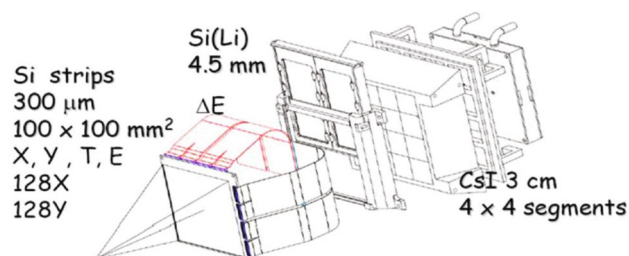


Fig. 9 Exploded view of the MUST2 telescope. This figure is from [38]



Fig. 10 (Color online) The SiHyBall annular detector (left) and the octagonal barrel (right). This figure is from [37]

Despite the good detection performances of the silicon detectors, it is still sometimes necessary to detect coincidental γ -rays for a better determination of energy levels or distinguishing long-lived isomeric states. For example, in a $d(^{34}\text{Si}, p)^{35}\text{Si}$ experiment [44] performed at GANIL, the energies and angles of the recoil protons were measured with four modules of the MUST2 array, while a more accurate energy determination of the bound excitation levels populating the ^{35}Si was achieved by analyzing the γ -ray energy spectrum measured by four segmented high-purity germanium (HpGe)detectors in the EXOGAM array. An isomer-tagging technique was used for distinguishing the long-lived isomeric states by directly measuring the cross section of the 0_2^+ state of ^{12}Be that is populated by the reaction $d(^{11}\text{Be}, p)$ [3]; the delayed-correlation technique was also employed in the study of μs -isomers of ^{67}Ni [45]. The detection of γ -ray plays a key role in numerous single-nucleon transfer reactions [3, 45, 46].

A combined view of the silicon and high-purity germanium detection array at GANIL is shown in Fig. 11. This setup was used for the $d(^{16}\text{C}, p)^{17}\text{C}$ experiment [47].

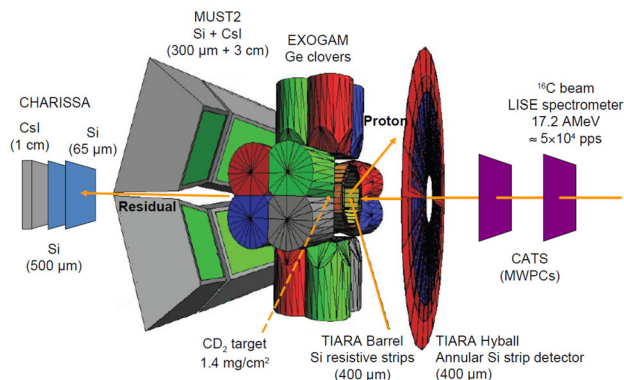


Fig. 11 (Color online) A combined view of the detector arrays at GANIL. This figure is from [47]

Similar arrays have also been constructed at other facilities. Several (d, p) transfer reactions in inverse kinematics have been performed at REX-ISOLDE, CERN using a combination of silicon detectors and γ -ray detectors, for the purpose of studying the single-particle properties at the border of the island of inversion [48] or around traditional magic numbers. For example, in the ^{79}Zn [49] and ^{67}Ni [45] experiments, the setup (see Fig. 12), which was composed of the T-REX array [50] and Miniball [51], allowed the combined detection of protons recoiling from the (d, p) reaction and γ -rays emitted from the residual nuclei. The high-resolution Miniball, which consists of 24 six-fold segmented HpGe crystals, has been used at REX-ISOLDE for over ten years. An overview of the technical details of the full Miniball setup is given in [52]. The silicon detector array T-REX was designed to be used in combination with Miniball, providing the positions (or angles) and the $\Delta E - E$ PID of light particles.

The silicon detector arrays that were developed at HRIBF at Oak Ridge National Laboratory are named ORRUBA [53], and SuperORRUBA [54]. The latter is an upgrade of the former. These arrays are geometrically similar; however, the former uses position sensitive resistive silicon strip detectors, like those utilized in TIARA and T-REX, while double-sided silicon strip detectors are applied in the upgraded array, which have better energy (and positional) resolution because of the increase in the number of electronics channels. A schematic view of ORRUBA is shown in Fig. 13. Focusing on the evolution of nuclear structure away from the stability line and the astrophysical r -processes that occur during supernova, the capability of measuring the transfer reactions in inverse kinematics on unstable nuclei has been tested in several

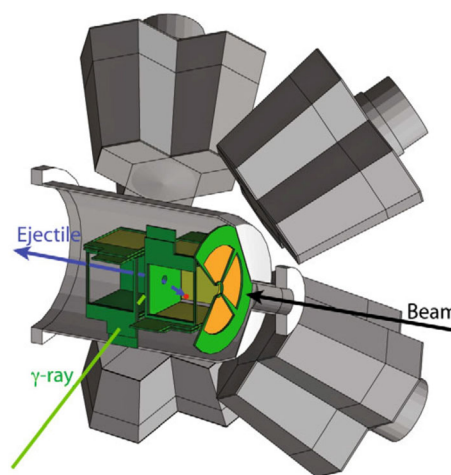


Fig. 12 (Color online) The schematic layout of T-REX and Miniball. The left side of the MINIBALL array, vacuum chamber, and particle detectors is removed for improved visualization. This figure is from [50]

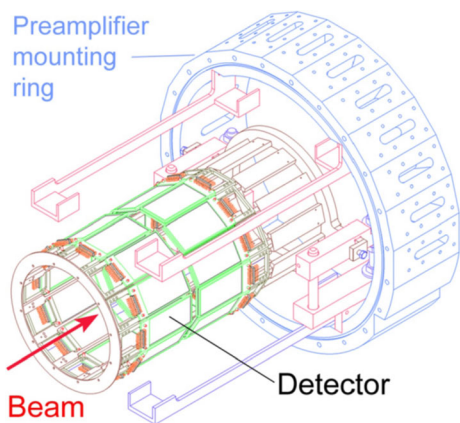


Fig. 13 (Color online) A schematic view of ORRUBA. The assembly is mounted on an annular chamber. This figure is from [54]

experiments [11, 55, 56]. Both of these arrays can be used in combination with GAMMASPHERE [57] or GREINA [58] in order to obtain high-resolution excitation energy spectra.

The high-resolution array (HiRA) [59] was developed at NSCL at a similar time to the construction of ORRUBA. Similar to LASSA [60], the HiRA array uses a combination of silicon detectors and CsI(Tl) crystals for PID. Like MUST2, HiRA is not designed specifically for transfer reactions in inverse kinematics. However, the HiRA array is useful for measuring transfer reactions because of its energy, angular resolution, and large acceptance. For example, in the study of ^{33}Ar [61] and ^{55}Ni [62], the excitation energy spectrum was successfully reconstructed from the recoil light particles measured with the HiRA array by coincidentally detecting the residual with the S800 spectrometer. Figure 14 shows HiRA under use in a transfer reaction.

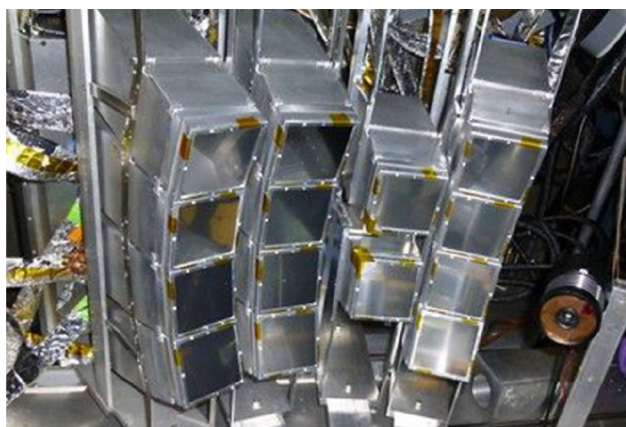


Fig. 14 (Color online) The high-resolution array (HiRA). In this figure, HiRA is placed at the forward angle for a measurement of transfer reaction. This figure is from [66]

Similar to TIARA, ORRUBA, and T-REX, SHARC [63] is a silicon detector array used at TRIUMF for the transfer reaction. SHARC can be used in conjunction with the γ -ray detector array TIGRESS [64], as seen in Fig. 15. With highly segmented silicon detectors, SHARC provides a better angular resolution than the other three arrays. The charged-particle reaction spectroscopy station IRIS [65] was also developed at TRIUMF in order to perform transfer reactions and the inelastic scattering of rare isotopes for use in inverse kinematics. Besides the regular silicon detectors and CsI crystals, IRIS also provides a thin solid hydrogen/deuteron target that is formed by freezing the hydrogen/deuteron gas onto an Ag foil that has been cooled to 4 K.

The detection of the aforementioned γ -rays was achieved with the use of HpGe detectors. HpGe detectors have good energy resolution but low intrinsic detection efficiency, which leads to low statistics in the coincidence measurement of the recoil particles and the γ -rays. Two methods that do not involve increasing the beam intensity are usually used to solve this problem. One is to increase the γ -ray detection efficiency by using other detectors with higher efficiency, such as NaI. This method was employed by RIKEN for the study of drip-line nuclei. Although RIKEN can produce radioactive beams with some of the highest beam intensities in the world, the production of adequate statistics remains problematic. For example, in a study of the near drip-line nucleus ^{23}O with $d(^{22}\text{O}, p)$ reaction [67] and the $d(^{22}\text{O}, d\gamma)$ reaction [68], the total intensity of the secondary beam was only approximately 1500 counts per second (cps), with an average ^{22}O intensity of 600 cps. Adequate statistics are difficult to produce using the HpGe detector, so a γ -ray detection array DALI2 comprised of NaI crystals was employed. The experimental setup is shown in Fig. 16. The residuals were analyzed

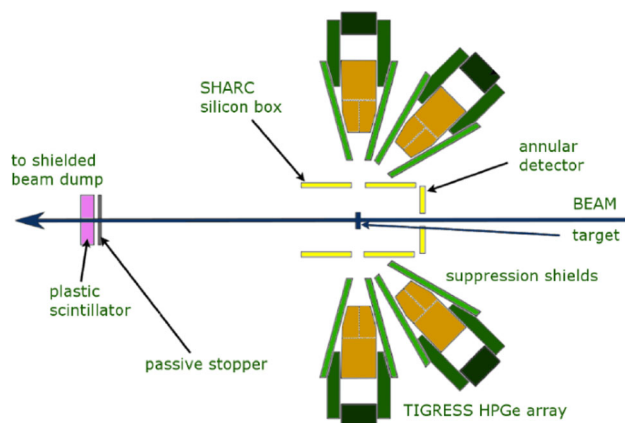


Fig. 15 (Color online) Schematic view of the experimental setup composed of the silicon detection array SHARC and the γ -ray detection array TIGRESS. This figure is from [17]

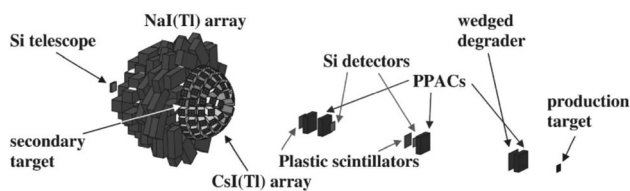


Fig. 16 Schematic view of the experimental setup in RIKEN for the $d(^{22}\text{O}, p)$ reaction. This figure is from [67]

using RIPS, while the recoil light particles were measured using 156 CsI(Tl) scintillation crystals. DALI2 [69], with 20% a full-energy photon peak efficiency for 1 MeV γ -rays, was placed around the target in order to detect the γ -rays from the excited states of ^{22}O that were produced via inelastic scattering [68]. The MUST2 array was also used at RIKEN in order to detect and identify recoil particles; for instance, the $d(^{11}\text{Li}, ^3\text{He})^{12}\text{Be}$ experiment presented in [40].

No detection arrays are currently available at the EN-course terminal at the Research Center of Nuclear Physics (RCNP) in Osaka university [70]. Therefore, it is an ideal place for users to build their own detection systems for different physical goals using silicon detectors and γ -ray detectors. Figure 17 shows the experimental setup inside the large scattering chamber for the $d(^{11}\text{Be}, p)^{12}\text{Be}$ experiment which was carried out at 26.9 MeV/nucleon [3]. The telescopes TELE0 and TELE1, which are comprised of silicon detectors and CsI crystals, were used for the detection of residual nuclei and scattered light particles, respectively. The annular double-sided silicon strip detector (ADSSD) is responsible for the measurement of recoil protons produced in transfer reactions, and the PID is

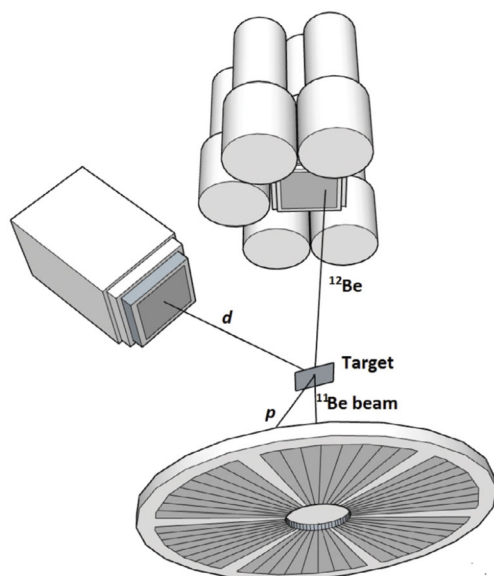


Fig. 17 Schematic view of the experimental setup for $d(^{11}\text{Be}, p)^{12}\text{Be}$, performed at RCNP. This figure is from [3]

achieved using the TOF- ΔE method. The scintillation counters, composed of NaI and BGO scintillators, were used to discriminate the isomeric state of ^{12}Be from other bound excited states. A similar setup was also applied for the $d(^{14}\text{B}, p)^{15}\text{B}$ experiment, which investigated the s -wave intruder components in the low-lying states of ^{15}B . This experimental setup was also employed for the $d(^{16}\text{C}, ^3\text{He})^{15}\text{B}$, and the $d(^{15}\text{C}, ^3\text{He})^{14}\text{B}$ experiments, which were performed at the radioactive beam line at Lanzhou (RIBLL1) in 2018 and 2019, respectively.

4.2 Active-target time projection chamber

With the improvement in the detection techniques used to measure recoil particles, one major contribution to the uncertainties in the excitation energy spectrum comes from the energy loss inside the target. For exotic nuclei that are far from the β stability line, the low intensity and low-energy features of the secondary beam make it difficult to conduct transfer reaction experiments with the traditional plastic (CH_2) or deuterated polythene (CD_2) targets. The combination of a time projection chamber with a gaseous active target provides an alternative solution for studying nuclear systems that are weakly bound [71].

The MAYA detector [72], which is based on the concept of an active target, was developed at GANIL more than ten years ago, allowing the use of a relatively thick gaseous target without any loss in resolution by using the detection gas as the target material. The charged particles inside the detector ionize the filling gas along their trajectories and the released electrons drift toward the amplification area under a high electric field. The projection of the trajectory on one plane is obtained from the segmentation of the readout device, while that of the third dimension is derived from the measured drift time. The reconstruction of the three-dimensional trajectories becomes possible by the analysis of the pad signals and the drift time. The point of reaction can thus be derived. Fig. 18 shows the ionization process and detection principle of MAYA.

This kind of active-target time projection chamber (AT-TPC) is also a powerful tool that can be used to study elastic and inelastic scattering [73–76], without worrying about the low-energy scattered particles being stopped inside the target. A new-generation active-target device, ACTAR TPC [77, 78], is currently under construction at GANIL for the purpose of expanding the dynamical range, lowering the thresholds, and increasing the detection efficiency.

Other facilities are also making progress in the development of state-of-the-art detectors. The larger AT-TPC that was constructed at NSCL [79–81] can be used to measure longer trajectories of recoil particles. The test

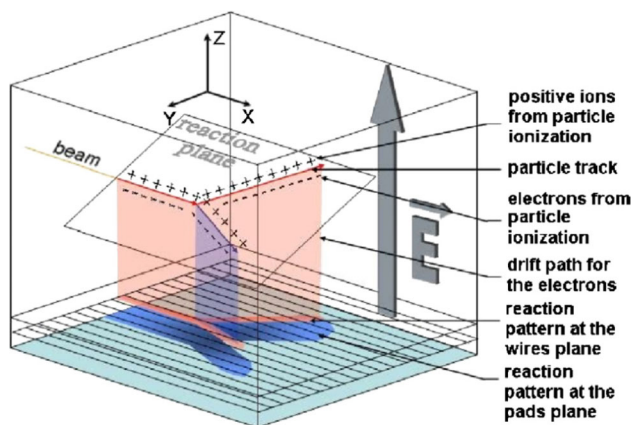


Fig. 18 (Color online) Schematic diagram of the ionization process and the detection principle of MAYA. This figure is from [72]

experiment with a ^{46}Ar beam shows the potential of this detector for investigating the single-particle states of nuclei that are far from the stability line. Figure 19 shows the schematic view of the AT-TPC at NSCL.

A compact AT-TPC, MAIKo, has recently been developed at RCNP, together with Kyoto University [82]. The elastic and inelastic scattering experiments of a radioactive beam of ^{10}C [83] on ^4He have been performed to test the performance of MAIKo [82]. This kind of advanced detector AT-TPC is also under development by the experimental group at Peking University [84], the Institute of Applied Physics in Shanghai [85], and the Institute of Modern physics in Lanzhou, China.

4.3 A new approach with a magnetic spectrometer

Unlike the traditional magnetic spectrometers that are used for measuring reactions in normal kinematics, a new type of helical orbit spectrometer, HELIOS [86, 87], has

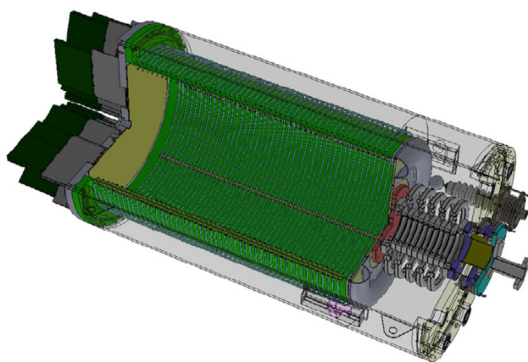


Fig. 19 (Color online) A schematic view of the AT-TPC at NSCL. The outer shielding is transparent in this image so that the details of the inner volume are visible. The beam enters the detector through the beam duct at the right-hand side of the image and moves toward the sensor plane on the left. This figure is from [80]

been developed at the Argonne National Laboratory. HELIOS, which was designed specifically to measure recoil light particles with high energy and position resolutions, has been used in several transfer reaction experiments in inverse kinematics [29, 88–90].

As the target and detectors are placed inside a uniform magnetic field, the charged particles emitted from the reaction travel on cyclotron orbits in the magnetic field, eventually reaching the beam axis again after one cyclotron period, where they are detected by silicon detectors, as seen in Fig. 20. By measuring the arrival time at the silicon array along the beam axis, which is independent of the energy and the scattering angle, the mass to charge ratio A/q can be obtained and the PID attained. For a fixed reaction Q -value, the energy of the emitting particle is proportional to the z position measured by the silicon arrays along the direction of the beam. Because of the lesser influence from the target thickness and the beam spot size, a better resolution can be achieved in terms of excitation energy, as discussed in [86]. In the $d(^{12}\text{B}, p)^{13}\text{B}$ [90] experiment, the resolution of HELIOS was sufficient to separate two closely spaced excited states at $E_x = 3.48$ MeV and 3.68 MeV in ^{13}B . Although this method encounters problems when measuring particles with the same A/q value, such as deuterons and α particles, it is adequate for most transfer reactions.

Because of the introduction of the magnetic field, the acceptance of the spectrometer is limited by the radius of the solenoid and the homogeneity of the magnetic field strength. Combination with γ -ray detectors remains a challenge because the light particles travel inside the volume where the γ -ray detectors are supposed to be placed.

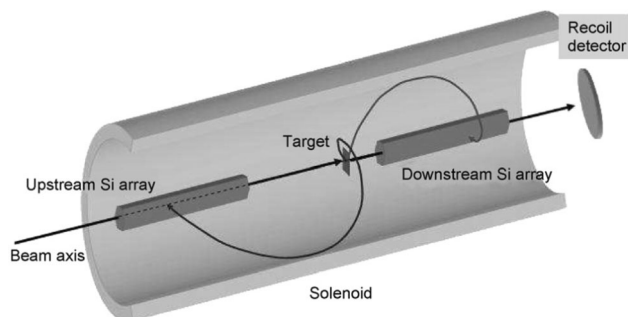


Fig. 20 HELIOS at the Argonne National Laboratory. This figure is from [86]

5 Experimental results of single-nucleon transfer reactions

In most light neutron-rich nuclei around $N = 8$, the ordering of the $2s_{1/2}$, $1p_{1/2}$, and $1d_{5/2}$ orbits is usually different from that of stable nuclei, resulting in the emergence of large amounts of s -wave intruder components and the formation of halos [13, 91], such as those seen in ^{11}Be , ^{11}Li , and ^{15}C . The breakdown of the $N = 8$ shell closure that is due to the $2s_{1/2}$ orbital intruding into the p shell is closely related to the appearance of the neutron halo in light neutron-rich isotopes. It is therefore important that the influence of the $2s_{1/2}$ orbital around $N = 8$ is studied systematically.

Table 2 summarizes the intruder s -wave intensities in the ground-state wave functions of loosely bound nuclei around $N = 8$ from various experiments, together with their single-neutron separation energies (S_n). It is worth noting that the ground states of most nuclei with smaller S_n ($S_n \leq 1.22$ MeV), such as ^{11}Be and ^{15}C , have predominant s -wave components; however, nuclei that contain at least one extra neutron S_n ($S_n \geq 3.17$ MeV), ^{12}Be and ^{16}C have few such components. In addition to ^{11}Be and ^{15}C , ^{14}B is another nucleus with smaller S_n and a dominant s -wave component [30, 92–95], which indicates that the $2s_{1/2}$ orbit intrudes into the $1d_{5/2}$ orbital in the ground state of ^{14}B . It is therefore worth questioning how much of the s -wave component is seen in the ground state of its adjacent isotope ^{15}B . Intruding components have also been observed in other $N = 10$ isotones during several experiments, such as the $2n$ removal reaction in ^{14}Be [96] and the $1n$ transfer reaction in ^{16}C [29].

Transfer reactions, especially the single-nucleon transfer reaction, can provide useful spectroscopic information for

understanding the evolution of the nuclear shell structure by precisely detecting unusual components such as the intruder s -wave. Various single-nucleon transfer reaction experiments carried out using light exotic nuclei in inverse kinematics are reviewed in the next section, focusing on the spectroscopic study of neutron-rich He, Li, Be, B, and C isotopes (including bound and unbound nuclei) around $N = 8$. The results obtained from other kinds of reaction, such as breakup reactions, charge exchange reactions, and knockout reactions are not presented in this paper.

5.1 Helium isotopes

^8He

The “double-borromean” nucleus ^8He [102] is an interesting subject with the largest neutron-to-proton ratio among all the known particle-stable nuclei, exhibiting a neutron halo or thick neutron skin. ^8He is therefore an excellent candidate for testing different models describing nuclear structure [103]. Its neighbors, ^7He and ^9He , are particle unbound; thus, it offers an opportunity to study the shell evolution of nuclear structures as a function of the increasing numbers of neutrons. The charge radius of ^8He is smaller than that of ^6He because of the isotropic distribution of the four valence neutrons [104], which is different from the traditional concept. With four loosely bound valence neutrons, ^8He is a unique system that can be used to investigate the role of correlations that occur between neutrons such as pairing [105, 106].

The ground state of ^8He is still an ambiguous topic, attracting attention experimentally as well as theoretically. The cluster orbital shell model approximation (COSMA) assumes that ^8He is comprised of a ^4He core with four valence neutrons filling the $1p_{3/2}$ sub-shell [107]. This assumption is equal to that of pure jj coupling. The analysis of the $p(^8\text{He}, t)$ reaction at incident energies of 15.7 and 61.3 MeV/nucleon [103] consistently indicates that the ground-state wave function of ^8He deviates from the pure $(1p_{3/2})^4$ structure. This result is in agreement with the theoretical calculation produced by Hagino’s group [108], which concludes that the probability of the $(1p_{3/2})^4$ and $(1p_{3/2})^2(1p_{1/2})^2$ configurations in the ground-state wave function of the ^8He nucleus are 34.9% and 23.7%, respectively. The asymmetry molecule dynamics (AMD) calculation also suggests that the ground state of ^8He has both the jj coupling feature ($^4\text{He} + 4n$) and the LS coupling feature ($^4\text{He} + 2n + 2n$) [109]. The “ $t + t +$ valence neutrons” structure [110] and “di-neutron” structure [111] are also predicted by the AMD model for the ground state of neutron-rich He isotopes. The contributions from the first 2^+ excited state of ^6He and the cluster of ^5H to the

Table 2 Summary of the intruder s -wave strength in the ground-state wave functions of weakly bound nuclei around $N = 8$, together with their single-neutron separation energies (S_n)

Isotope	s -wave strength	S_n (MeV)
^{11}Li	47% [97–99]	0.396
^{11}Be	71% [11]	0.504
^{12}Be	19% [3]	3.17
^{14}Be	87% [96]	1.78
^{13}B	little [90, 100]	4.88
^{14}B	71–89% [30, 92–95]	0.97
^{15}B	no data	2.78
^{15}C	88% [101]	1.22
^{16}C	30% [29]	4.25

ground-state configuration of ${}^8\text{He}$ have also been investigated using a $p({}^8\text{He}, t)$ transfer reaction with an incoming energy of 25 and 61.3 MeV/nucleon [112, 113]. Early in 2001, a heavy hydrogen ${}^5\text{H}$ was observed via the $p({}^6\text{He}, 2p){}^5\text{H}$ reaction at 32 MeV/nucleon. By using triple $2p$ - t coincidences, the ${}^5\text{H}$ ground state was identified as a resonance state at 1.7 ± 0.3 MeV above the $n + n + t$ threshold, with a width of 1.9 ± 0.4 MeV [114].

The transfer reaction is a sensitive and powerful probe that can be used to determine the properties of atomic nuclei [115]. The neutron SF extracted from the $p({}^8\text{He}, d){}^7\text{He}$ reaction includes the structural information of ${}^8\text{He}$ and ${}^7\text{He}$. The ground state of ${}^7\text{He}$ is a resonant state which often immediately decays into ${}^6\text{He} + n$, while the excited state of ${}^7\text{He}$ at $E_x = 2.9 \pm 0.3$ MeV usually decays into $3n + {}^4\text{He}$ [116]. Deuterons that are coincidental with ${}^6\text{He}$ and ${}^4\text{He}$ in the reaction channel $p({}^8\text{He}, d){}^7\text{He}_{g.s.}$ and $p({}^8\text{He}, d){}^7\text{He}_{E_x=2.9\text{MeV}}$, respectively, are therefore often measured. The ratio of the $2n$ to $1n$ transfer cross section for ${}^8\text{He}$ is expected to be sensitive to the correlations that occur among the valence neutrons [108, 117]. Calculations carried out using the translational invariant shell model (TISM) suggest that the SFs ratio of $p({}^8\text{He}, t){}^6\text{He}_{g.s.}$ to $p({}^8\text{He}, t){}^6\text{He}^{2+}$ depends strongly on the assumed structure of the ${}^8\text{He}$ ground state [112, 113]. It is worth mentioning that this ratio is quite close to 1.0 under the pure jj coupling assumption but deviates from 1.0 for mixed jj and LS coupling. The ${}^6\text{He}$ ground state with a half-time of 806.70 ms can be directly measured; however, its 2^+ excited state immediately decays to ${}^4\text{He} + 2n$. Experimentally, the coincidence of $t + {}^4\text{He}$ is usually observed in the $p({}^8\text{He}, t){}^6\text{He}^{2+}$ reaction.

The DCSs of the reactions $p({}^8\text{He}, d){}^7\text{He}_{g.s.}$ and $p({}^8\text{He}, d){}^6\text{He}^{2+}$ were measured at the relatively high incident energy of 82.3 MeV/nucleon in an experiment performed at RIKEN by the nuclear physics experimental group associated with Peking University. The results of $p({}^8\text{He}, d){}^7\text{He}_{g.s.}$ are shown in Fig. 21. These results were analyzed using FR-ADWA [11] with FRESKO code [18]. Although little difference was found between the SFs extracted because of the choice of different OP parameters, the values are all significantly smaller than 4.0. This may indicate that the ground-state wave function of ${}^8\text{He}$ is not a pure jj coupling or $(1p_{3/2})^4$ configuration, and there is a possibility that other configurations such as $(1p_{3/2})^2(1p_{1/2})^2$ may occur. The $p({}^8\text{He}, t){}^6\text{He}^{2+}$ channel is prior to the $p({}^8\text{He}, t){}^6\text{He}_{g.s.}$ channel at 82.3 MeV/nucleon, which is also observed at incident energies of 25 [112] and 61.3 [113] MeV/nucleon. Analysis of all the existing (p, t)

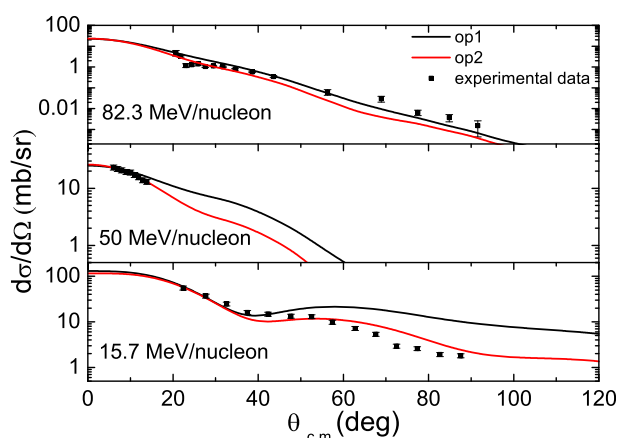


Fig. 21 (Color online) Compared with the theoretical calculations, the experimental DCSs of ${}^8\text{He}(p, d){}^7\text{He}_{g.s.}$ reaction at incoming energies of 82.3, 50 [116] and 15.7 MeV/nucleon [118]. The black line represents the initial FR-ADWA calculation result without any parameter adjustment. If imaginary part of the depth of the $d + {}^7\text{He}$ single-folding potential increases by a factor of 2.0, the results are shown as the red solid lines

reaction data with large angular ranges in the CM frame consistently indicates that the ${}^5\text{H}$ cluster transfer is necessary for reproducing the angular distributions at angles larger than 90° . Thus, the structure of the cluster ${}^8\text{He} = {}^5\text{H} + {}^3\text{H}$ should not be neglected when investigating the ground state of ${}^8\text{He}$. All the ratios of $p({}^8\text{He}, t){}^6\text{He}_{g.s.}$ to $p({}^8\text{He}, t){}^6\text{He}^{2+}$ that are extracted from the existing (p, t) reaction data deviate from 1.0, which is inconsistent with the hypothesis of four valences filling a closed $1p_{3/2}$ sub-shell.

${}^9\text{He}$

As aforementioned, besides the model where four valence neutrons fill the $1p_{3/2}$ shell in the ground state of ${}^8\text{He}$, other configurations such as $(1p_{3/2})^2(1p_{1/2})^2$ may occur. For example, the ground state of ${}^9\text{He}$, with one more valence neutron than ${}^8\text{He}$ is possible. Some theoretical calculations predict that, with the same neutron number, the ground state of ${}^9\text{He}$ is particle unbound and may show the same parity inversion observed in the neighboring ${}^{11}\text{Be}$ and ${}^{10}\text{Li}$ (see the subsection below). However, in a no core shell model calculation [119], it is found that the ${}^9\text{He}$ ground-state resonance has a negative parity and thus breaks the parity-inversion mechanism observed in the ${}^{11}\text{Be}$ and ${}^{10}\text{Li}$ nuclei.

The unbound nuclear system ${}^9\text{He}$ was investigated through the $d({}^8\text{He}, p)$ transfer reaction by Golovkov et al. using a ${}^8\text{He}$ beam [120] at a laboratory energy of 25 MeV/nucleon. The lowest resonant state of ${}^9\text{He}$ was found at 2.0 MeV with a width of approximately 2.0 MeV, which came mainly from the experimental energy resolution of

approximately 0.8 MeV. The angular correlation pattern observed can be uniquely explained by the interference of the $(1/2)^-$ resonance with a virtual $(1/2)^+$ state and with a $(5/2)^+$ resonance at an energy of ≥ 4.2 MeV. However, the experimental energy resolution of approximately 800 keV prevents this conclusion because of the strong disagreement with a previous two-proton knockout reaction experiment [121], which suggested that a ground-state of ${}^9\text{He}$ has $J^\pi = 1/2^+$.

The same reaction was also performed at GANIL with the ${}^8\text{He}$ beam [39] at a laboratory energy of 15.4 MeV/nucleon. The MM spectrum was deduced from the kinetic energies and the emission angles of protons detected by four MUST2 telescopes. This MM spectrum displays a structure that lies just above the threshold for neutron emission, which is identified as the ground state of ${}^9\text{He}$. Despite the limited statistics describing the angular distribution of the state that was observed close to the ${}^8\text{He} + n$ threshold (180 ± 85 keV above), the result supports the conclusion that the ground state spin-parity of ${}^9\text{He}$ is $(1/2)^+$. This result confirms both the parity inversion and the s -wave intrusion. The first excited state lies approximately 1.3 MeV above the neutron threshold and is compatible with $J^\pi = (1/2)^-$, while simultaneously exhibiting a strongly mixed nature.

5.2 Lithium isotopes

${}^{10}\text{Li}$

The study of the unbound system ${}^{10}\text{Li}$ is of great interest as knowledge of this system is necessary for a theoretical description of the Borromean nucleus ${}^{11}\text{Li}$ [122]. The existence of a low-lying virtual intruder s -state has also been predicted by some theoretical models. However, because of the unbound nature of ${}^{10}\text{Li}$, the experimental study of these nuclei encounters numerous challenges, such as the coincidence detection of the neutron and ${}^9\text{Li}$.

Two different $d({}^9\text{Li}, p){}^{10}\text{Li}$ transfer reactions in inverse kinematics were performed separately at REX-ISOLDE [123] and NSCL [124]. The results of the former experiment [123] supported the existence of a low-lying (s) virtual state, with a (negative) scattering length and a $p_{1/2}$ resonance with an energy of $E_r \simeq 0.38$ MeV. However, the results of the latter experiment [124] were inconclusive as to the possible presence of a low-lying virtual state in ${}^{10}\text{Li}$ because of the poor statistics produced. The low amount of statistics and the poor energy resolution have always prevented definitive conclusions concerning the structures of ${}^{10}\text{Li}$. The results from these two experiments were therefore re-examined [125]. From this analysis, it was concluded that both measurements can be described

consistently using the same model for the $n - {}^9\text{Li}$ interaction and the seemingly different features can be understood if the different incident energy and angular range covered by the two experiments is taken into consideration. The s -wave virtual state in ${}^{10}\text{Li}$ was found to play a key role in the experiment using the lower beam energy; however, the excitation energy below $E_x < 1$ MeV was found to be dominated by the $p_{1/2}$ resonance in the higher energy experiment.

Most recently, a new $d({}^9\text{Li}, p){}^{10}\text{Li}$ transfer reaction in inverse kinematics was performed at TRIUMF with a much higher beam intensity (10^6 pps), which guaranteed the production of more statistics [126]. The ${}^{10}\text{Li}$ energy spectrum, which was analyzed using three Fano functions, is shown in Fig. 22. The comparison between the experimental data and the theoretical predictions, including the pairing correlation, clearly indicates the presence of a $p_{1/2}$ resonance (purple dashed line in Fig. 22) at the excitation energy of 0.45 ± 0.03 MeV. However, there is no obvious evidence for a significant s -wave contribution (blue dotted line) close to the threshold energy. Two high-lying resonances at 1.5 and 2.9 MeV were also observed. The corresponding angular distributions indicate a significant $s_{1/2}$ partial wave contribution (blue dotted line) for the 1.5 MeV resonance and a mixing of configurations at $E_x = 2.9$ MeV

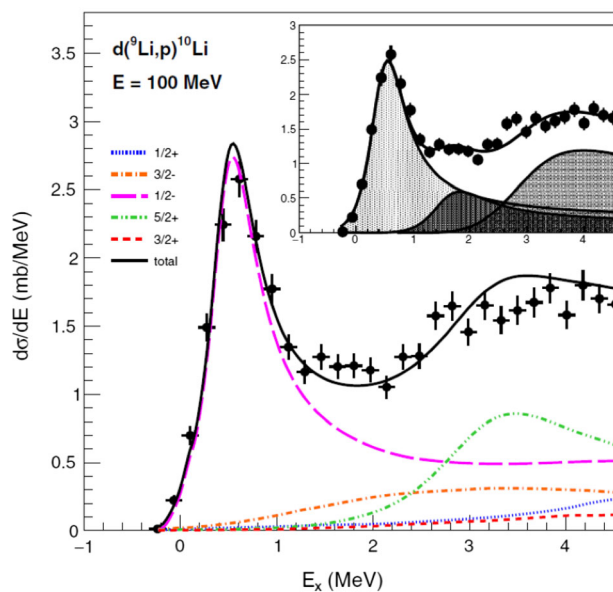


Fig. 22 (Color online) ${}^{10}\text{Li}$ energy spectrum rebuilt from the recent $d({}^9\text{Li}, p){}^{10}\text{Li}$ reaction. The curves show the partial wave contributions obtained from theoretical prediction, including the effects of a pairing correlation. The solid black line represents the sum of the contributions from each partial wave. The inset picture is the best-fitting sum of the three Fano functions combined with the experimental energy resolution. This figure is from [126]

for the first time, with the $d_{5/2}$ partial wave (green dot-dashed line) contributing significantly to the cross section.

Several other kinds of experiments have been carried out. Although the excitation energy, parity, and spin assignments are controversial, it can be concluded that the ground state of ^{10}Li contains a valence neutron in a $2s_{1/2}$ state at approximately 50 keV or below [13]. This conclusion is different from that obtained from the aforementioned transfer reactions, which might be attributed to the difficulty of a coincidence measurement between ^9Li and a proton for such a low-energy resonance using the transfer reaction.

^{11}Li

In order to study the configurations of the ground state of ^{11}Li , a $p(^{11}\text{Li}, d)^{10}\text{Li}$ reaction was performed at TRIUMF using a solid hydrogen target and a 5.7 MeV/nucleon ^{11}Li beam [127]. Only one resonance was observed, at $E_r = 0.62 \pm 0.04$ MeV with a width of 0.33 ± 0.07 MeV. The elastic scattering was measured along with the transfer reaction in order to obtain the OP parameters for the entrance channel. The angular distribution of $p(^{11}\text{Li}, d)^{10}\text{Li}$ to $E_r = 0.62$ MeV is best reproduced by assuming that the neutron is removed from the $1p_{1/2}$ orbital, as shown by the red solid curve in Fig. 23. A SF of 0.67 ± 0.12 is determined for the $(1p_{1/2})^2$ component. This result is much less than that predicted by the conventional shell model (≈ 2.0), confirming a relatively small $(p_{1/2})^2$ component in the ground state of ^{11}Li . Assuming the remaining probability fraction to be s - and d -waves, a large

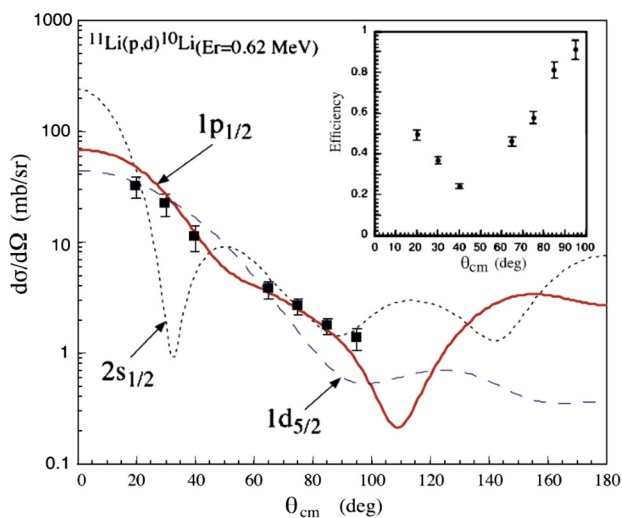


Fig. 23 (Color online) The angular distribution for $^{11}\text{Li}(p, d)^{10}\text{Li}_{E_r=0.62\text{ MeV}}$. The solid (red) curve, dashed (blue) curve, and dotted (black) curve represent the DWBA calculations with an assumption that one neutron is removed from the $1p_{1/2}$, $1d_{5/2}$, and $2s_{1/2}$ orbital, respectively. The detection efficiency is shown in the inset. This figure is from [127]

$(2s_{1/2})^2$ probability fraction $\geq 44\%$ is deduced for the ground state of ^{11}Li . This data is also theoretically analyzed in [128], in which the similar $p_{1/2}$ -wave component of 31% is given.

Recently, a $d(^{11}\text{Li}, ^3\text{He})$ reaction was performed at RIKEN in inverse kinematics with a radioactive beam of ^{11}Li at 50 MeV/nucleon [40]. This reaction was used to study the configurations of the ground state of ^{11}Li . Two peaks were observed at 1.4(3) and 6.3(7) MeV when the MM spectrum was gated onto the ^8He residuals. The angular distributions of the ^3He nuclei in coincidence with ^8He residues shown in Fig. 24 were analyzed using the DWBA calculations. The OPs for the entrance channel of $^{11}\text{Li} + d$ were obtained from the elastic scattering data that were collected from the same experiment. Use of the DWBA might not be appropriate for dealing with the unbound ^{10}He . It is therefore argued that the removal of a deeply bound proton in the reaction justifies the simplification of the reaction model. The $\langle^{11}\text{Li}|^{10}\text{He}\rangle$ overlap function used in the DWBA calculations was calculated from the standard potential model (SPM), source term approach (STA), and the STA, corrected with the

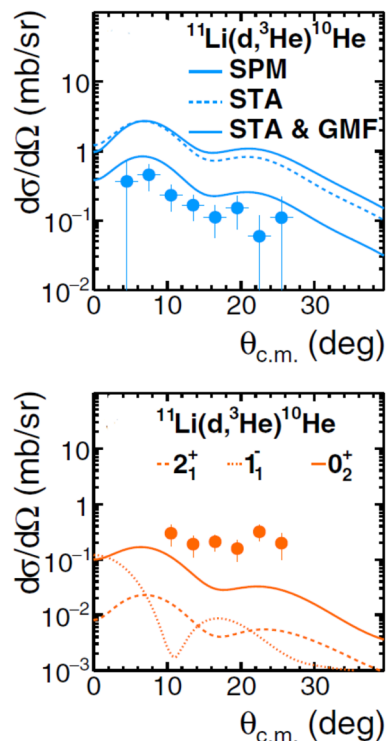


Fig. 24 (Color online) Experimental $(d, ^3\text{He})$ cross sections for populating the ground state (up) and excited state (down) of $^{10}\text{He}_{g.s.}$ in comparison with the DWBA calculations. SPM, STA, and STA-GMF are used to describe different overlap functions used in the DWBA calculations. Further details can be found in [40], which is also the source of this figure

geometrical mismatch factor (GMF). The shape of the angular distribution is reproduced sufficiently; however, the magnitude of the cross section for the ground state of ^{10}He is overestimated in all three cases. The cross sections for the excited states are greater than those predicted by the DWBA calculations with the assumed SFs from the shell model calculations for the 2_1^+ , 1_1^- , 0_0^+ states in ^{10}He . The experimental results may be attributed to the important contribution of a ^{10}He core excitation in the ground-state wave function of ^{11}Li .

The ground state of ^{11}Li was also studied using a $2n$ transfer reaction, $p(^{11}\text{Li}, t)^9\text{Li}$ [99], with a radioactive beam of ^{11}Li at an extremely low incidental energy of 3 MeV/nucleon. The experiment was performed [99] at TRIUMF using the active-target detector MAYA. Multi-step transfer calculations were applied with different wave functions of ^{11}Li . Only the wave functions with a strong mixture of p and s neutrons and three-body correlations were found to provide the best fit to the magnitude of the DCSs.

5.3 Beryllium isotopes

^{11}Be

The beta decay experiment of ^{11}Be [129] indicates that the spin-parity of the ground state of ^{11}Be is $1/2^+$ [130] instead of $1/2^-$, which means that the last neutron prefers to take the $2s_{1/2}$ orbital instead of the $1p_{1/2}$ orbital. The disappearance of the $N = 8$ shell closure has been proposed as an explanation for this phenomenon in neutron-rich light nuclei. A spectroscopic study of a $d(^{10}\text{Be}, p)$ reaction that was carried out at Oak Ridge National Laboratory with a radioactive beam of ^{10}Be at four different incident energies indicated that the average SF for a neutron in an $nlj = 2s_{1/2}$ state coupled to the ground state of ^{10}Be is 0.71 ± 0.05 [11]. This large SF indicates a significant s -wave strength in the ground-state of ^{11}Be .

In addition to the naive $n \otimes ^{10}\text{Be}(0_{\text{gs}}^+)$ component, the ground-state wave function of ^{11}Be was found to have a considerable overlap with that of a valence neutron coupled to an excited $^{10}\text{Be}(2^+)$ core via a (p, d) transfer reaction with a ^{11}Be beam [101, 131, 132]. In the former configuration, the valence neutron surrounding the inert core ^{10}Be populates the intruder s orbital rather than the normal p orbital. However, in the latter, the ^{10}Be is excited to the 2^+ state at 3.37 MeV and the valence neutron fills the intruder d orbital. The s - and d -wave components in the ground state of ^{11}Be were calculated as 84% and 16%, respectively, from the (p, d) transfer reaction with the beam energy at 35.3 MeV/nucleon [101, 131, 132]. The results

were confirmed by the same reaction with a radioactive ^{11}Be beam at 26.9 MeV/nucleon [133].

^{12}Be

With one more neutron, the valence-nucleon configuration of ^{12}Be has also attracted much attention. Two valence neutrons may populate the d orbital as well as the s and p orbitals, which is different from the situation seen in ^{11}Li . However, which component is dominant? This question has been investigated through several $d(^{11}\text{Be}, p)$ reactions.

In the $d(^{11}\text{Be}, p)$ reaction performed at TRIUMF [27], the s -wave neutron fraction of the first two 0^+ levels in ^{12}Be was investigated for the first time. In this experiment, three peaks were observed in the excitation energy spectrum, including the ground state and a 1^- state located at 2.71 MeV, as well as an unresolved doublet that was constructed from the 0_2^+ and 2^+ states. Angular distributions for each peak in the excitation energy spectrum were analyzed using the DWBA method using global optical model potentials as well as parameters from the neighboring nuclei. The ground state s -wave SF was determined to be $0.28_{-0.07}^{+0.03}$ while that of the long-lived 0_2^+ excited state was $0.73_{-0.40}^{+0.27}$. The value for the 0_2^+ state has a large uncertainty, because this state was not clearly distinguished from the 2^+ state. The result has been questioned by Fortune et al. [134], as it is inconsistent with the results from knockout experiments and theoretical calculations.

The same reaction was studied with a lower beam energy (2.8 MeV/nucleon) at the REX-ISOLDE facility [135]. Besides the outgoing proton measured by the T-REX silicon detector array, the γ -rays emitted from the excited states of ^{12}Be were also detected using the MINIBALL germanium array. The γ -ray detection enabled a clear identification of the four known bound states in ^{12}Be , and the angular distribution of each state has been studied individually. In this case, the SF for the ground state is also smaller than that of the excited 0_2^+ state. This experiment suffered from an extremely low beam energy, leading to ineffective detection in the most sensitive angular range, especially for the 0_2^+ state.

It would be difficult to compare the SF results of the two aforementioned transfer reactions with other results or with each other [16] because of the lack of proper normalization procedures. With the purpose of further studying the intruder configuration in ^{12}Be , a new measurement of the $d(^{11}\text{Be}, p)$ reaction was performed at the EN-course beam line, RCNP, with special measures taken to deal with the questioned experimental uncertainties of the two previous experiments [3]. Figure 17 is a schematic view of the experimental setup. A special isomer-tagging method was used to discriminate the 0_2^+ state from the broad excitation

energy peak. Fig. 25a shows the measured proton energies versus the laboratory angles, gated onto the ^{12}Be in the zero-degree silicon detector. Fig. 25b gives the excitation energy spectrum of ^{12}Be , deduced from the energies and angles of the recoil protons. The elastic scattering of the $^{11}\text{Be} + p$ was measured simultaneously in order to estimate the hydrogen contamination in the $(\text{CD}_2)_n$ target and to obtain a reliable OP to be used in the analysis of the transfer reaction. The FR-ADWA calculations were employed to extract the SFs of the low-lying states in ^{12}Be . Figure 26 compares the experimental and theoretical cross sections. The extracted s -wave SFs are $0.20^{+0.03}_{-0.04}$ and $0.41^{+0.11}_{-0.11}$ for the 0_1^+ and 0_2^+ states, respectively. The ratio between the SFs of the first two low-lying 0^+ states,

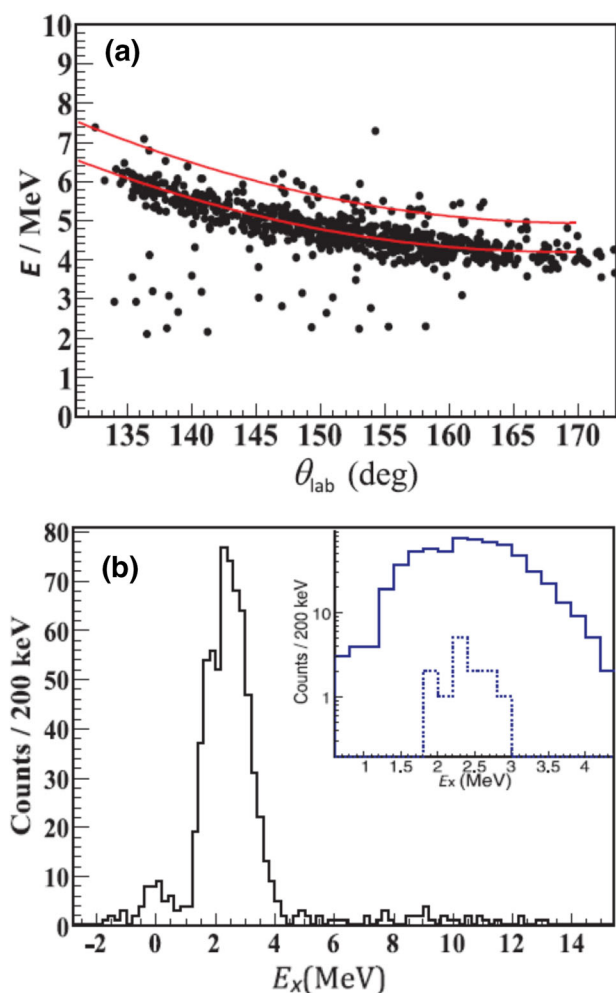


Fig. 25 (Color online) **a** The measured proton energies versus the laboratory angles, gated onto the ^{12}Be in the zero-degree silicon detector. The red solid lines illustrate the calculated kinematics of the $d(^{11}\text{Be}, p)$ transfer reaction to the ground state and the 2.251 MeV excited state. **b** The excitation energy spectrum of ^{12}Be deduced from the recoil protons in **a**. The dotted curve in the inset shows the events during coincidence with the 0.511 MeV γ rays detected by the scintillation counters. This figure is from [136]

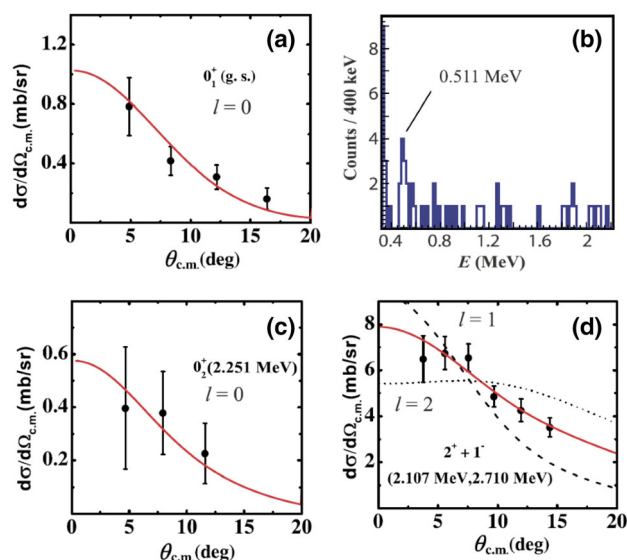


Fig. 26 (Color online) Experimental DCSs of the $^{11}\text{Be}(d, p)$ reaction with a radioactive beam of ^{11}Be at 26.9 MeV/u (solid dots), together with the FR-ADWA calculations (curves), for **a** the g.s. (0_1^+), **c** the isomeric state (0_2^+), and **d** the summed 2^+ and 1^- states. l in **a**, **c**, and **d** denote the transferred orbital angular momentum into the final state of ^{12}Be . **b** is dedicated to the γ -ray energy spectrum in coincidence with the $^{12}\text{Be} + p$ events. This figure is from [3]

together with the previously reported results for the p -wave components, was used to deduce the single-particle intensities in these two bound 0^+ states of ^{12}Be , which can be compared directly with the shell model predictions. The s -, d -, p -wave intensity for the 0_1^+ and 0_2^+ states are calculated as 0.19 ± 0.07 , 0.57 ± 0.07 , 0.24 ± 0.05 , and 0.39 ± 0.02 , 0.02 ± 0.02 , 0.59 ± 0.05 , respectively. The error bars are deduced from the statistic uncertainties of the SFs. The results show a small s -wave (0.19 ± 0.07) with a dominant d -wave (0.57 ± 0.07) intruding into the ground state of the ^{11}Be when dominated by an intruder s -wave. The experimental results are compatible with those obtained from previous measurements of the transfer reaction, considering the reported uncertainties.

In principle, there should be three 0^+ states observed within the ^{12}Be in this $p - sd$ model space. Until now, only the lowest two have been found in the bound region, and the third 0^+ has not been identified experimentally. More studies, such as $^{13}\text{B}(d, ^3\text{He})^{12}\text{Be}$ or $^{14}\text{B}(d, ^4\text{He})^{12}\text{Be}$, are encouraged to further investigate the excited states of ^{12}Be .

5.4 Boron isotopes

For the $N = 8$ system, as aforementioned, the halo nucleus ^{11}Li has a large s -wave component in its ground-state wave function. In contrast, a larger s -wave component

was observed in the 0_2^+ isomeric state rather than the 0_1^+ ground state in ^{12}Be . However, the shell structure of the ^{13}B nucleus has not been discussed. Its ground state has $J^\pi = 3/2^-$, and the properties of its low-lying positive-parity states can reveal significant amounts of information about the $2s_{1/2}$ and $1d_{5/2}$ single-particle energies and the residual interaction. For the $N = 9$ isotones, ^{12}Li and ^{13}Be are particle unbound; however, ^{14}B with $S_n = 0.97$ MeV is loosely bound. Therefore, the lightest particle-bound $N = 9$ isotope, ^{14}B , provides a unique opportunity to study the evolution of the properties of single-neutron states, especially the gap between the $2s_{1/2}$ and $1d_{5/2}$ orbitals. The $N = 10$ isotones are ideal for studying two-neutron interactions in the sd shell. From the knockout experiment, it was found that the ground state of ^{14}Be is dominated by a s -wave (87%) [96]. From the $^{15}\text{C}(d, p)$ transfer reaction, the 0_1^+ ground state of ^{16}C was found to be dominated by a d -wave [29]. Since ^{15}B is between ^{14}Be and ^{16}C , the questions arise whether the percentage of the s -wave component in the ground-state wave function of $^{13,14,15}\text{B}$ could be ascertained, and whether s -waves dominate in their low-lying states. Several transfer reaction experiments have been carried out to answer these questions.

$^{12,13}\text{B}$

The experiment investigating the $d(^{11,12}\text{B}, p)$ transfer reaction to the low-lying states of $^{12,13}\text{B}$ was performed at Argonne using a silicon detector [100]. The excitation energy spectra for ^{12}B (upper) and ^{13}B (lower), which were constructed using the recoil protons in coincidence with ^{12}B and ^{13}B , are shown in Fig. 27. The overall Q -value resolution is approximately 250 keV (FWHM), which is not sufficient for the discrimination of the doublet state at $E_x = 3.482$ and 3.681 MeV in ^{13}B . This doublet is expected to contain both s - and d -wave components.

A new experiment concerning the $d(^{11,12}\text{B}, p)$ transfer reaction to the low-lying states of $^{12,13}\text{B}$ was performed at Argonne with the HELIOS setup [90], in which the properties of some of the low-lying states in the neutron-rich $N = 8$ nucleus ^{13}B were studied [90]. Two closely spaced states at $E_x = 3.482$ and 3.681 MeV were observed in ^{13}B that could be clearly identified from each other, benefiting from the better energy resolution of HELIOS. The angular distributions are shown in Fig. 28. The state at 3.48 MeV shows $l = 0$ angular distribution and the spin-parity is assigned as $(1/2)^+$. The angular distribution of the state located at a 3.68 MeV excitation energy exhibits a $l = 2$ shape. $J^\pi = (5/2)^+$ can be tentatively assigned, based on comparison with the shell model calculations.

The absolute normalization of the cross sections was not possible because the absolute beam intensity was not measured in this experiment. Only the relative SFs are

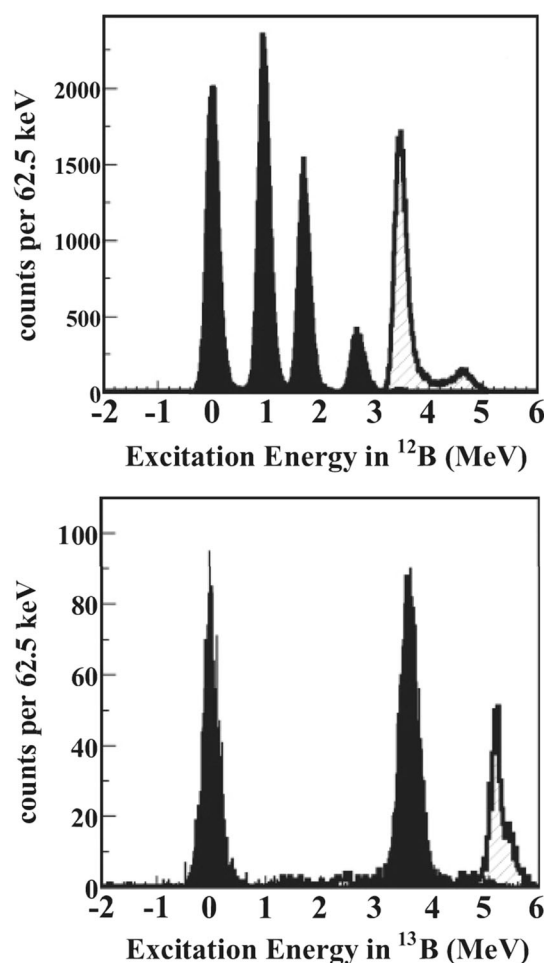


Fig. 27 The excitation energy spectra for ^{12}B (upper) and ^{13}B (lower) from the $d(^{11}\text{B}, p)$ and $d(^{12}\text{B}, p)$ transfer reactions, respectively [100]. The solid and dashed shadows describe the bound and unbound excited states, which were constructed from the recoil protons coincidental with ^{12}B (^{13}B) and ^{11}B (^{12}B) in the upper (lower) figure, respectively

meaningful. As shown in Fig. 29, the relative SF of the suggested $(5/2)^+$ state, when compared with that of the $(1/2)^+$ state, is smaller than the value predicted by the shell model. More d -wave strength is expected at excited states above 4 MeV in ^{13}B . The absolute excitation energies, as well as the ordering of the excited states, are also not in good agreement with the shell model predictions as can be seen in Fig. 29. The $(3/2)^+$ state that was predicted is not observed below 4.8 MeV, which may correspond to a strong transition at 5.1 MeV that was observed in a prior measurement (the lower picture in Fig. 27) [100]. More positive-parity states are expected to exist at energies above that of neutron separation; therefore, further experimental studies are required in this area.

A state at $E_x = 4.83$ MeV is strongly populated in the $^4\text{He}(^{12}\text{Be}, ^{13}\text{B}\gamma)$ reaction with a secondary beam of ^{12}Be at

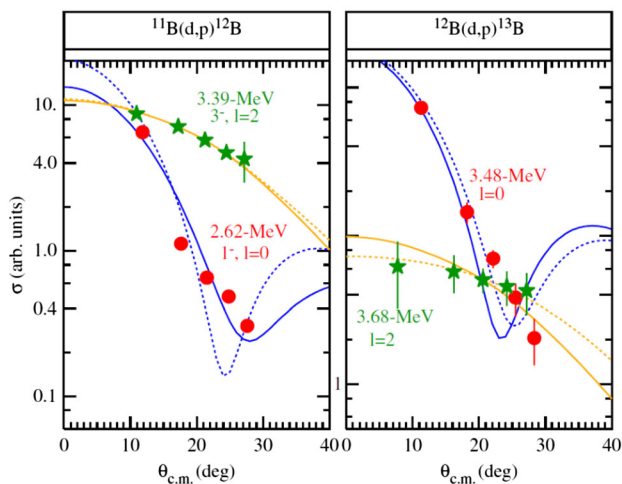


Fig. 28 (Color online) The left-hand and right-hand figures show the angular distributions of the $^{11}\text{B}(d, p)^{12}\text{B}$ and $^{12}\text{B}(d, p)^{13}\text{B}$ reactions, respectively, for two states known to be populated with $l = 0$ and $l = 2$. The solid and the dashed lines are the DWBA calculations that were carried out with two different sets of parameters [90]

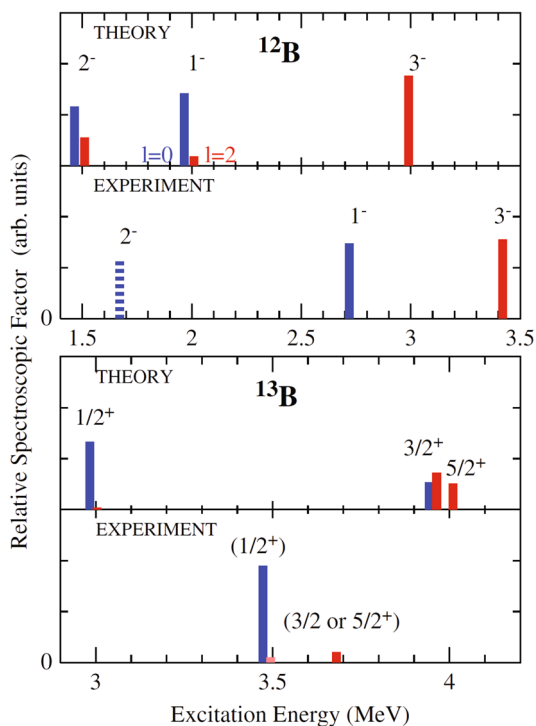


Fig. 29 (Color online) The relative SF for $l = 0$ (blue bars) and $l = 2$ (red bars) of the $d(^{11}\text{B}, p)^{12}\text{B}$ (upper) and $d(^{12}\text{B}, p)^{13}\text{B}$ (lower) reactions compared with the shell model calculations. Solid bars are experimental values from the measurement in [90], while the dashed bar is from [100]

50 MeV/nucleon [137]. The spin and parity of this state were assigned to $1/2^+$ by comparing the DCSs data with the DWBA calculations, see Fig. 30. The DWBA predictions with $\Delta l = 0, 1$, and 2 are shown as the red solid, green

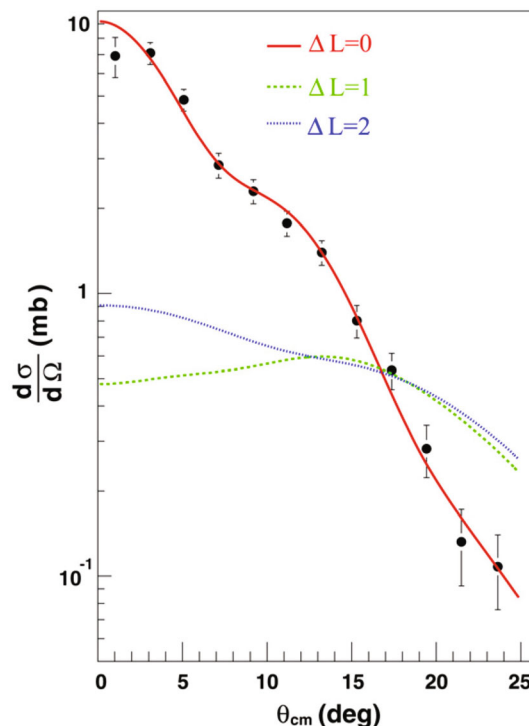


Fig. 30 (Color online) Angular distributions of the $^4\text{He}(^{12}\text{Be}, ^{13}\text{B}\gamma)$ reaction to the $E_x = 4.83$ MeV resonant state. The optical model potentials for the entrance and exit channels are obtained from the folding model [137]

dashed, and blue dotted curves in Fig. 30. The angular distributions, especially the peak observed at the forward angles, are well described by the $\Delta l = 0$ DWBA calculations. This is therefore interpreted as a proton intruder state. Another $2p\text{-}2h$ state at $E_x = 3.53$ MeV in ^{13}B , with a tentatively assigned spin-parity of $3/2^-$, is also suggested to be a neutron intruder state [138].

^{14}B

The experimental data of the $d(^{13}\text{B}, p)^{14}\text{B}$ reaction using HELIOS confirm that the ground and first excited states are predominantly populated by s -waves and are single-neutron halo states [30]. The normalized SFs for the low-lying states are shown in Table 1, suggesting that the 2^- ground state has a moderate $2s_{1/2} - 1d_{5/2}$ configuration mixing and the 1^- first excited state is nearly pure $2s_{1/2}$. The effective single-particle energies of the $2s_{1/2}$ and $1d_{5/2}$ neutron orbitals in ^{14}B show the inversion of these two orbitals compared to the normal ordering in the valley of stability [30]. Figure 31 shows the excitation energy spectrum of ^{14}B obtained in this experiment. The 2^- and 1^- states, which are expected to be comprised of one $1p_{3/2}$ valence proton (hole) coupled with one $1d_{5/2}$ valence neutron, were not observed. However, unbound 3_1^- and 4_1^- states were measured that were composed of the same coupling of $\pi(1p_{3/2})^{-1}v(1d_{5/2})^1$.

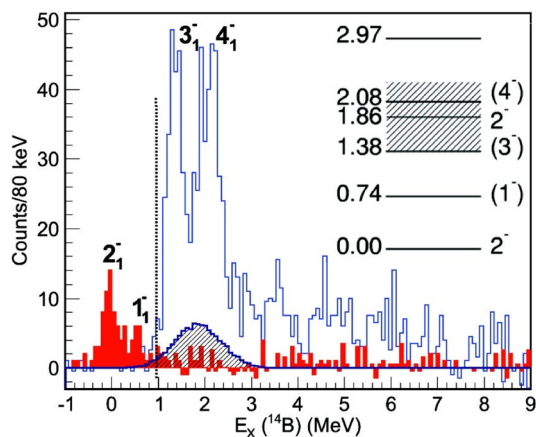


Fig. 31 (Color online) ^{14}B excitation energy spectrum from the $d(^{13}\text{B}, p)^{14}\text{B}$ reaction. The filled (open) histogram corresponds to protons detected in coincidence with the identified $^{14}\text{B}(^{13}\text{B})$ recoil ions. The vertical dashed line shows the neutron separation energy. The inset shows the level diagram for ^{14}B [30]

$(d, ^3\text{He})$ experiments were also carried out with HELIOS, using ^{14}C and ^{15}C secondary beams to provide spectroscopic information about the final states in ^{13}B and ^{14}B [95]. Several transitions were observed in the ^{14}C data, which were reproduced sufficiently using the transferred angular momentum of $l = 1$. This result indicates that the ground state of ^{14}C likely possesses a $1p_{1/2}$ proton character. A weak $l = 0$ transition was also measured, which may be associated with a possible $1/2^+$ proton intruder state in ^{13}B [137]. It is worth noting that such an excitation is not well described by shell model calculations. The ground state (2_1^-) and the first excited state (1_1^-) at $E_x = 0.654\text{ MeV}$ in ^{14}B could not be discriminated from each other in the ^{15}C data, because of the inferior energy resolution for ^3He produced by HELIOS. In addition to the bound states, a broad unbound excited 2_2^- state was observed clearly by the $d(^{15}\text{C}, ^3\text{He})$ reaction at approximately $E_x = 1.8\text{ MeV}$ in ^{14}B , which was not seen but was expected in the previous $d(^{13}\text{B}, p)^{14}\text{B}$ experiment [30]. Figure 32 shows the angular distributions of $^{15}\text{C}(d, ^3\text{He})$ to the bound $2_1^- - 1_1^-$ doublet and the unbound 2_2^- state in ^{14}B . All the DCSs are reasonably well described by a $l = 1$ proton removal from ^{15}C . The relative SFs extracted from this experiment are consistent with both the shell model calculations and expectations based on prior measurements of the $d(^{13}\text{B}, p)^{14}\text{B}$ reaction.

^{15}B

Previous experiments have shown a large s -wave component in the ground state of ^{14}B . With an extra neutron, this poses an interesting question about how much s -wave component exists in the ground state and low-lying excited states of its adjacent isotope ^{15}B ; however, there is no

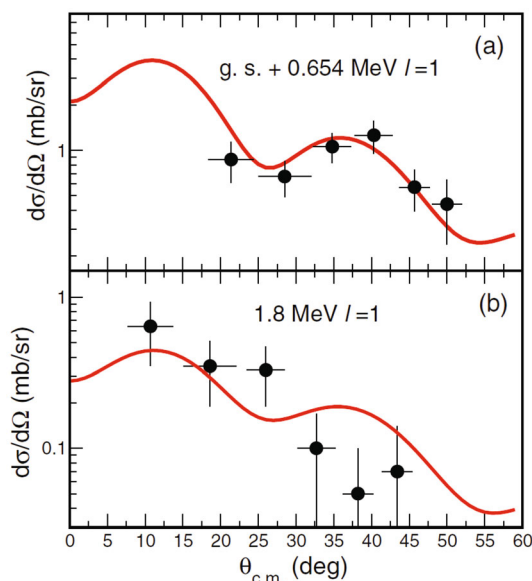


Fig. 32 (Color online) Angular distribution of the $^{15}\text{C}(d, ^3\text{He})$ reaction to $2_1^- - 1_1^-$ doublet (a) and the 2_2^- state at $E_x = 1.8\text{ MeV}$ (b) in ^{14}B [95]

experimental data available that can be used to address this question. Recently, $(d, ^3\text{He})$ and (d, p) transfer reactions in inverse kinematics were performed in order to study the spectroscopic information of ^{15}B . In principle, there should be two $J^\pi = (3/2)^-$ states, including the ground state, in ^{15}B because of the mixture of s - and d -wave components. However, the second $(3/2)^-$ has not yet been found experimentally. The s -wave SFs of the known states, including the ground state of ^{15}B are unknown. In theory, the shell model predicted a small s -wave SF of 0.48 for the ground state [13], which was significantly smaller than the expected value of 2.0, which implies that there is a larger s -wave SF present in the excited $(3/2)^-$ state, as seen in the situation surrounding ^{12}Be and ^{16}C .

A $d(^{16}\text{C}, ^3\text{He})^{15}\text{B}$ experiment was recently conducted at RIBLL1 in Lanzhou, China. The preliminary result of the light-particle PID is shown in Fig. 33. It was found that some ^3He particles clearly recoil from the transfer reaction under coincidence with ^{15}B . Further analysis of the data collected from this experiment is in progress.

Shortly after the $(d, ^3\text{He})$ experiment, a $d(^{14}\text{B}, p)^{15}\text{B}$ experiment was performed at RCNP, which used a similar setup to that shown in Fig. 17. The elastic scattering of ^{14}B on the proton and deuteron targets were measured using data from the same experiment in order to extract OPs for the theoretical calculations of the transfer reaction. The energy versus angle for protons and deuterons emitted from the elastic scattering channels are shown in Figs. 34 and 35, respectively. The protons from the transfer reaction were measured with a single-layer annular silicon detector

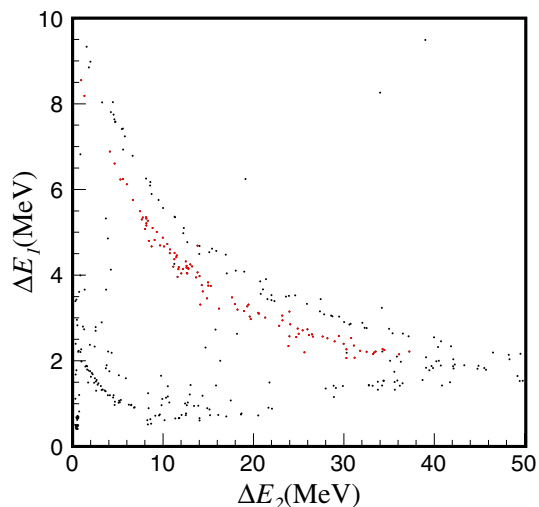


Fig. 33 (Color online) Particle identification of the light particle in coincidence with ^{15}B detected at zero degrees. ^3He particles are shown as red dots

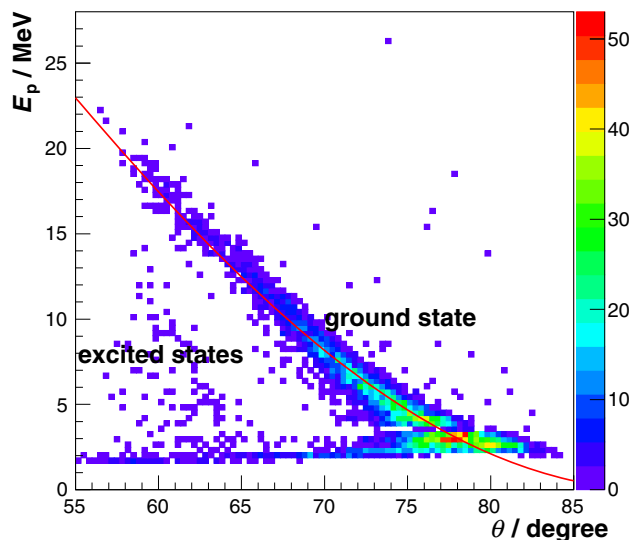


Fig. 34 (Color online) Energy versus angle for protons scattered elastically from ^{14}B . The red line shows the calculated kinematic curve

at the backward angle, and the PID was achieved using the TOF- ΔE method. As shown in Fig. 36, the proton from the transfer reaction is clearly distinguished from other particles emerging from the fusion-evaporation reaction between the ^{14}B and the silicon detectors in the zero-degree telescope.

5.5 Carbon isotopes

The intruder components have been studied for the neutron-rich Li, Be, and B isotopes via transfer reactions. The experimental studies on carbon isotopes are discussed

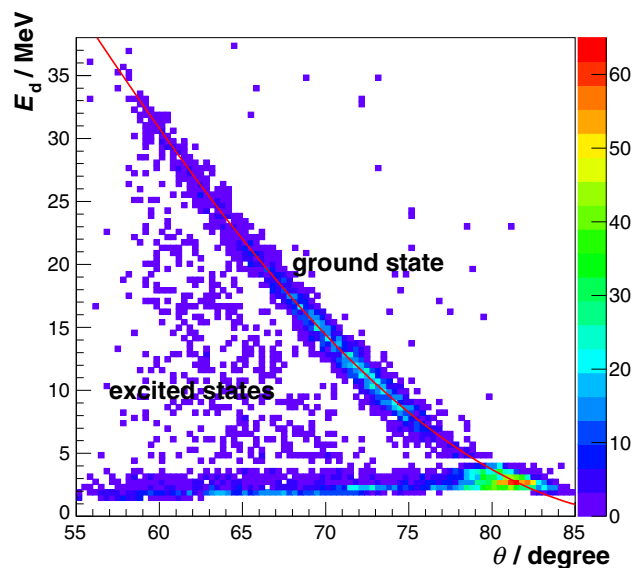


Fig. 35 (Color online) Energy versus angle for the elastic scattering of $^{14}\text{B} + d$. The red line shows the calculated kinematic curve for this reaction

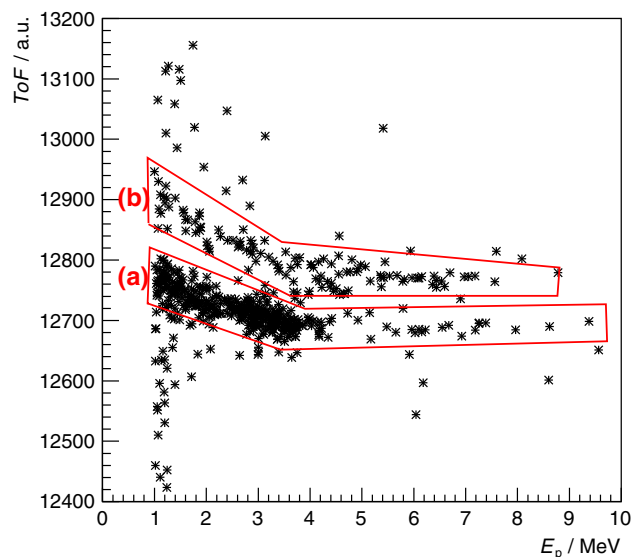


Fig. 36 (Color online) Particle identification by the annular silicon detector using the TOF- ΔE method. **a** Protons from the transfer reaction. **b** Protons from the fusion-evaporation reaction between the secondary beam ^{14}B and the silicon detectors placed at approximately zero degrees relative to the beam line

next. With 8 neutrons filling the p shell and the high excitation energy of (6.09 MeV) for the first excited (2^+) state, ^{14}C shows a good magic character for $N = 8$. However, the spin-parity of the ^{15}C ground state is $(1/2)^+$, which clearly indicates that the $2s_{1/2}$ orbital is below the $1d_{5/2}$ orbital. Studies of the $^{14}\text{C}(d, p)^{15}\text{C}$ reaction [139] show that the ground state of ^{15}C is well described as a valence neutron in a single-particle state around a ^{14}C core,

with an *s*-wave SF as large as 0.88. It is also indicated that the ground state of ^{15}C has only a small fraction of the $^{14}\text{C}(2^+) \times d$ configuration [140]. This component is similar to the core excitation component in the ground state of ^{11}Be .

However, the study of the $d(^{15}\text{C}, p)^{16}\text{C}$ reaction [29] shows a different picture, suggesting that ^{16}C may not need to be described with exotic phenomena. The $d(^{15}\text{C}, p)^{16}\text{C}$ reaction was carried out at Argonne National Laboratory. A highly thin deuterated polyethylene ($(\text{C}_2\text{D}_4)_n$) was bombarded by the ^{15}C beam with a high beam intensity of $1 \sim 2 \times 10^6$ pps. The recoil protons were detected with the HELIOS spectrometer. The 0_1^+ , 2_1^+ , and 0_2^+ states and a $2_2^+/3_1^-$ doublet in ^{16}C were observed in the excitation energy spectrum reconstructed with the recoil protons. Although a resolution of approximately 140 keV (FWHM) was used, it was still insufficient for resolving the closely spaced $2_2^+/3_1^-$ doublet near $E_x = 4$ MeV. The angular distributions for these four populated states are shown in Fig. 37, compared with the DWBA calculations using four sets of optical model parameters. Absolute SFs were obtained by comparing the experimental cross sections with the DWBA calculations. The absolute SFs were normalized by requiring that the SFs of the first two 0^+ states were summed to 2.0. The normalized *s*-wave SFs calculated for the first two 0^+ states were 0.60 ± 0.13 and 1.40 ± 0.31 . This result indicates that, similar to ^{12}Be , more *s*-wave components appear in the excited 0_2^+ state

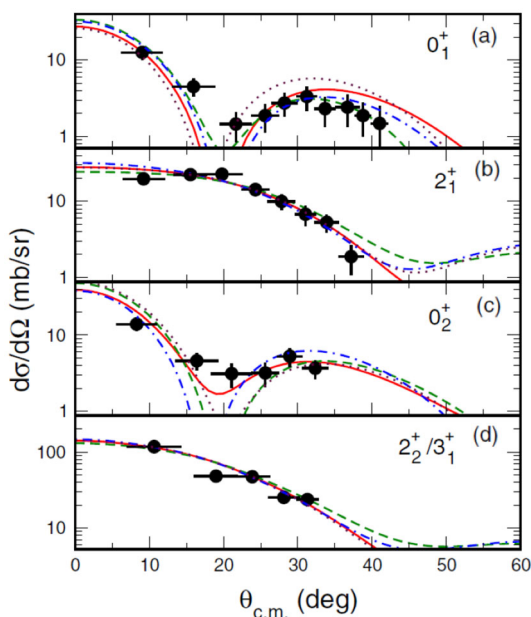


Fig. 37 (Color online) Angular distributions for the $^{15}\text{C}(d, p)$ reaction to the 0_1^+ (a), 2_1^+ (b), 0_2^+ (c) states and a $2_2^+/3_1^+$ doublet (d) in ^{16}C . The curves represent DWBA calculations with different OP parameters [29]

(70%) than in the 0_1^+ ground state (30%). The *s*-wave strength also indicates that each state has a large number of $(1s_{1/2})^2$ components, revealing a strong mixture of the $2s_{1/2}$ and the $1d_{5/2}$ orbital configurations in the low-lying states of ^{16}C . Note that the 30% *s*-wave component in the ground-state wave function of ^{16}C is much smaller than that of ^{15}C but much larger than that of ^{17}C , which is dominated by a *d*-wave. Further experimental studies, such as $d(^{16}\text{C}, ^3\text{He})^{15}\text{B}$, $d(^{17}\text{N}, ^3\text{He})^{16}\text{C}$, and $d(^{16}\text{C}, p)^{17}\text{C}$ [47] are required in order to explain the differences between these neutron-rich carbon isotopes.

5.6 Summary of experimental results

A brief summary of the experimental studies that have been carried out on the intruder components found within neutron-excess He, Li, Be, B, and C isotopes is provided in this subsection. The variation in the energy of the $2s_{1/2}$ orbital in the $N = 7$ and $N = 9$ systems, relative to the $1d_{5/2}$ orbital, is presented in Figs. 38 and 39, respectively. The order of the *s* and *d* orbitals is reversed in the $N = 7$ isotones, and the energy gap between these two orbitals decreases as Z increases. The *s* orbital also moves rapidly with respect to the *p* orbital for the $N = 7$ nuclei. The sequences of these two orbitals are inverted in ^9He and ^{11}Be but are reverted to the normal order in ^{12}B and ^{13}C . For $N = 9$ isotones, the effective single-particle energies for $2s_{1/2} = 2$ and $1d_{5/2} = 2$ orbitals relative to the one-neutron separation energy, clearly shows the inversion of *s* and *d*. Two valence neutrons are present in $N = 6$, $N = 8$, and $N = 9$ nuclei, meaning that the experimental studies of these isotopes are more complicated and the results are not generally conclusive, except for ^8He , ^{11}Li , ^{12}Be , and ^{16}C . Conclusions from these studies include the following. The

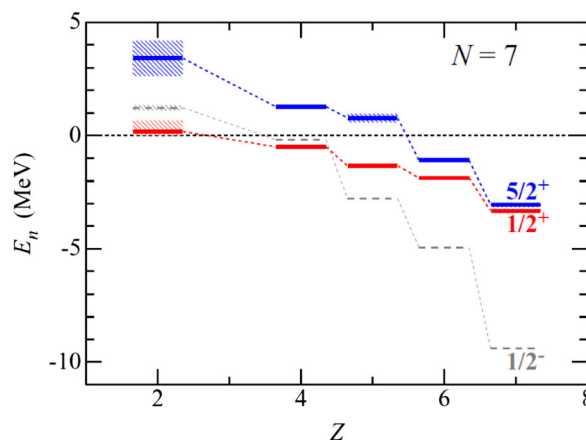


Fig. 38 (Color online) The experimental data available for the energy E_n , relative to the neutron threshold of the $1p_{1/2}, 1d_{5/2}$ and $2s_{1/2}$ orbitals for $N = 7$ nuclei. This figure is from [141]

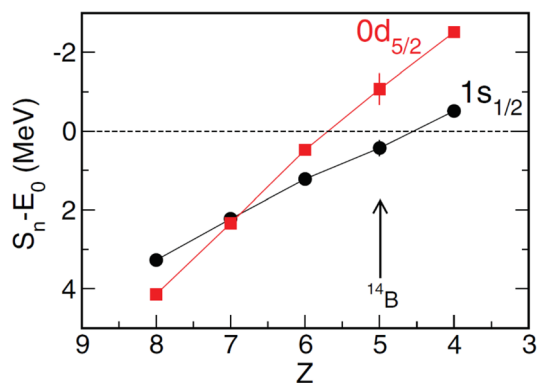


Fig. 39 (Color online) Effective single-particle binding energies for $N = 9$ isotones. This figure is from [30]

intruder $(1p_{1/2})^2$ component cannot be neglected in the ground state of ${}^8\text{He}$. In the ground state of ${}^{11}\text{Li}$, the intruder $(2s_{1/2})^2$ configuration is as important as the normal $(1p_{1/2})^2$ component. For ${}^{12}\text{Be}$ and ${}^{16}\text{C}$, the $(2s_{1/2})^2$ intrusion appears more in the excited 0_2^+ state than that in the 0_1^+ ground state. The core ${}^6\text{He}$ (${}^{10}\text{He}$) was found to be partially excited to the 2^+ state in the ground state of ${}^8\text{He}$ (${}^{11}\text{Li}$).

Some intruder configurations have also been found in the low-lying states of light neutron-rich nuclei from these transfer reactions. An exotic s -wave proton intruder state was observed at $E_x = 4.83$ MeV in ${}^{13}\text{B}$ using a proton transfer reaction of ${}^{12}\text{Be}$, which was re-examined using a new ${}^{14}\text{C}(d, {}^3\text{He})$ experiment. The positive-parity low-lying states in ${}^{13}\text{B}$, which are expected to be mixed with the $2s_{1/2}$ and $1d_{5/2}$ orbitals, have been studied in several $d({}^{12}\text{B}, p)$ experiments. Some of the strengths of the s - and d -waves that were found via the shell model predictions were not observed experimentally. The first excited state at $E_x = 0.74$ MeV in ${}^{14}\text{B}$ was most likely a s -wave halo state. The second $3/2^-$ state in ${}^{15}\text{B}$, which was similar to the 0_2^+ state in ${}^{12}\text{Be}$ and ${}^{16}\text{C}$, was predicted to be an s -wave dominant state but was not found in experiment. Two single-nucleon transfer reaction experiments, $d({}^{14}\text{B}, p)$ and $d({}^{16}\text{C}, {}^3\text{He})$, have been performed by the nuclear physics experimental group at Peking University in order to search for such an exotic state and study the intruder component in low-lying states of ${}^{15}\text{B}$; the data are currently under analysis, and there has been no conclusion as yet. These results clearly show that the experimental studies on the intruder component in light neutron-rich nuclei offers an opportunity to understand shell evolution in exotic nuclei.

The transfer reaction in inverse kinematics has also been used to study the shell evolution of nuclei around the conventional magic numbers $N = 20, 28, 50$, and 82 as well as the new magic numbers such as $N = 14, 16$, and 32 . Table 3 summarizes the recently reported transfer reaction

Table 3 A brief summary of the recently reported transfer reaction experiments focusing on heavier nuclei

Experiment	Facility	Year	Reference
$d({}^{15}\text{N}, p){}^{16}\text{N}$	ORNL	2008	[142]
$d({}^{14}\text{O}, t){}^{13}\text{O}$	GANIL	2013	[41]
$d({}^{14}\text{O}, {}^3\text{He}){}^{13}\text{N}$	GANIL	2013	[41]
$d({}^{16}\text{O}, p){}^{17}\text{O}$	CIAE	2019	[143]
$d({}^{19}\text{O}, p){}^{20}\text{O}$	ANL	2012	[31]
$d({}^{20}\text{O}, p){}^{21}\text{O}$	GANIL	2011	[42]
$d({}^{22}\text{O}, p){}^{23}\text{O}^*$	GANIL	2007	[67]
$d({}^{18}\text{F}, p){}^{19}\text{F}$	ANL	2018	[88]
$d({}^{21}\text{F}, p){}^{22}\text{F}$	ANL	2018	[144]
$d({}^{19}\text{Ne}, n){}^{20}\text{Na}$	FSU	2016	[55]
$d({}^{24}\text{Ne}, p){}^{25}\text{Ne}$	GANIL	2010	[46]
$d({}^{26}\text{Ne}, p){}^{27}\text{Ne}$	GANIL	2012	[145]
$d({}^{25}\text{Na}, p){}^{26}\text{Na}$	TRIUMF	2016	[146]
$d({}^{28}\text{Mg}, p\gamma){}^{29}\text{Mg}$	TRIUMF	2019	[147]
$d({}^{26}\text{Al}^m, p){}^{27}\text{Al}$	ANL	2017	[89]
$d({}^{34}\text{Si}, p){}^{35}\text{Si}$	GANIL	2014	[44]
$p({}^{34,46}\text{Ar}, d)$	NSCL	2010	[61]
$d({}^{44}\text{Ar}, p){}^{45}\text{Ar}$	GANIL	2008	[148]
$d({}^{46}\text{Ar}, p){}^{47}\text{Ar}$	GANIL	2006	[149]
$d({}^{60}\text{Fe}, p){}^{61}\text{Fe}^*$	GNAIL	2017	[43]
$p({}^{56}\text{Ni}, d){}^{55}\text{Ni}$	NSCL	2014	[62]
$d({}^{66}\text{Ni}, p){}^{67}\text{Ni}$	CERN	2014	[45]
$d({}^{66}\text{Ni}, p){}^{67}\text{Ni}$	CERN	2015	[150]
$d({}^{70}\text{Zn}, {}^3\text{He}){}^{69}\text{Cu}$	Alto	2016	[151]
$d({}^{72}\text{Zn}, {}^3\text{He}){}^{71}\text{Cu}$	GANIL	2015	[152]
$d({}^{78}\text{Zn}, p){}^{79}\text{Zn}$	CERN	2015	[49]
$d({}^{82}\text{Ge}, p){}^{83}\text{Ge}$	ORNL	2005	[153]
$d({}^{84}\text{Se}, p){}^{85}\text{Se}$	ORNL	2005	[153]
$d({}^{95}\text{Sr}, p){}^{96}\text{Sr}$	TRIUMF	2018	[154]
$d({}^{94,95,96}\text{Sr}, p)$	TRIUMF	2019	[155]
$d({}^{132}\text{Sn}, p){}^{133}\text{Sn}$	ORNL	2010	[156]
$d({}^{132}\text{Sn}, t){}^{131}\text{Sn}$	ORNL	2018	[157]
$p({}^{154,159}\text{Gd}, d)$	LBNL	2014	[158]

experiments focused on investigating heavier nuclei. The experimental results have been partly reviewed in [14]. In addition to shell evolution, these experiments were also used to study proton–neutron asymmetry, which is related to short-range correlations [159], and to provide the important reaction ratio for nuclear astrophysics; a summary in this regard can be found in [160].

6 Summary

The single-nucleon transfer reaction in inverse kinematics is a sensitive tool to investigate the exotic structure in unstable neutron-rich nuclei. The DCSs (or angular distributions) of the selectively populated final states contain essential structural information that can help understand the nature of the nuclear force and the interactions in unstable nuclei. The transferred momentum l (or the spin-parity of the low-lying states in the final nucleus), the SFs, and the effective single-particle energy can be deduced from the single-particle transfer reaction. These observations are useful for interpreting the shell evolution of neutron-excess nuclei. Inverse kinematics is preferred to normal kinematics in transfer reactions with radioactive beams. Several experimental setups including silicon detection arrays (with or without a γ -ray array), the special spectrometer HELIOS, and the newly developed AT-TPC, which are appropriate for use in single-nucleon transfer reactions in inverse kinematics, have been developed at various laboratories around the world. The basic modules, advantages, and disadvantages of each array are illustrated in this paper.

A large number of single-nucleon transfer reaction experiments have been carried out using radioactive beams in order to quantitatively study the intruder components in the low-lying states of neutron-rich He, Li, Be, B, and C isotopes. The experimental results are conclusive for the ground states of the $N = 7$ and $N = 9$ isotones. For example, the intruder s -wave component dominates in ${}^9\text{He}$, ${}^{10}\text{Li}$ (from other reactions), ${}^{11}\text{Be}$, ${}^{14}\text{B}$, and ${}^{15}\text{C}$. However, for the ground state of the $N = 6$, $N = 8$, and $N = 10$ isotones, the existence of two valence neutrons leads to more complications. Thus, although some experimental results are disputed, some of the intruder information on the ground state of ${}^8\text{He}$, ${}^{11}\text{Li}$, ${}^{12}\text{Be}$ and ${}^{16}\text{C}$ can be conclusive. First, the intruder $(1p_{1/2})^2$ component in ${}^8\text{He}$ cannot be ignored. The strength of the $(2s_{1/2})^2$ intrusion in ${}^{11}\text{Li}$, ${}^{12}\text{Be}$, and ${}^{16}\text{C}$ are 47%, 19%, and 30%, respectively, while the intensities of $(1p_{1/2})^2$ in ${}^{11}\text{Li}$ and $(1d_{5/2})^2$ in ${}^{12}\text{Be}$ and ${}^{16}\text{C}$ are greater than 50%. The s -wave intrusions were also found in some excited states, such as the proton intruder state in ${}^{13}\text{B}$, the first excited state in ${}^{14}\text{B}$, and the second 0^+ states in ${}^{12}\text{Be}$ and ${}^{16}\text{C}$. All these experimental studies and conclusions are helpful in explaining the anomalous behavior of the conventional magic number $N = 8$ in light neutron-rich nuclei. With further development of accelerators and detection techniques, it is anticipated that more single-particle transfer reactions will be performed in the future.

References

1. M.G. Mayer, On closed shells in nuclei. II. Phys. Rev. C **75**, 1969 (1949). <https://doi.org/10.1103/PhysRev.75.1969>
2. O. Haxel, J. Hans, D. Jensen et al., On the “magic numbers” in nuclear structure. Phys. Rev. C **75**, 1766 (1949). <https://doi.org/10.1103/PhysRev.75.1766.2>
3. J. Chen, J.L. Lou, Y.L. Ye et al., A new measurement of the intruder configuration in ${}^{12}\text{Be}$. Phys. Lett. B **781**, 412–416 (2018). <https://doi.org/10.1016/j.physletb.2018.04.016>
4. T. Otsuka, R. Fujimoto, Y. Utsuno et al., Magic numbers in exotic nuclei and spin-isospin properties of the NV interaction. Phys. Rev. Lett. **87**, 082502 (2001). <https://doi.org/10.1103/PhysRevLett.87.082502>
5. T. Otsuka, T. Suzuki, R. Fujimoto et al., Evolution of nuclear shells due to the tensor force. Phys. Rev. Lett. **95**, 232502 (2005). <https://doi.org/10.1103/PhysRevLett.95.232502>
6. T. Otsuka, T. Matsuo, D. Abe, Mean field with tensor force and shell structure of exotic nuclei. Phys. Rev. Lett. **97**, 162501 (2006). <https://doi.org/10.1103/PhysRevLett.97.162501>
7. T. Otsuka, T. Suzuki, M. Honma et al., Novel features of nuclear forces and shell evolution in exotic nuclei. Phys. Rev. Lett. **104**, 012501 (2010). <https://doi.org/10.1103/PhysRevLett.104.012501>
8. T. Otsuka, T. Suzuki, J.D. Holt et al., Three-body forces and the limit of oxygen isotopes. Phys. Rev. Lett. **105**, 032501 (2010). <https://doi.org/10.1103/PhysRevLett.105.032501>
9. A. Ozawa, T. Kobayashi, T. Suzuki et al., New magic number, $N = 16$, near the neutron drip line. Phys. Rev. Lett. **84**, 5493 (2000). <https://doi.org/10.1103/PhysRevLett.84.5493>
10. R. Kanungo, A new view of nuclear shells. Phys. Scr. **T152**, 014002 (2013). <https://doi.org/10.1088/0031-8949/2013/T152/014002>
11. K.T. Schmitt, K.L. Jones, A. Bey et al., Halo nucleus ${}^{11}\text{Be}$: a spectroscopic study via neutron transfer. Phys. Rev. Lett. **108**, 192701 (2012). <https://doi.org/10.1103/PhysRevLett.108.192701>
12. T. Aumann, A. Navin, D.P. Balamuth et al., One-neutron knockout from individual single-particle states of ${}^{11}\text{Be}$. Phys. Rev. Lett. **84**, 35 (2000). <https://doi.org/10.1103/PhysRevLett.84.35>
13. I. Tanihata, H. Savajols, R. Kanungo, Recent experimental progress in nuclear halo structure studies. Prog. Part. Nucl. Phys. **68**, 215–313 (2013). <https://doi.org/10.1016/j.pnpnp.2012.07.001>
14. K. Wimmer, Nucleon transfer reactions with radioactive beams. J. Phys. G **45**, 033002 (2018). <https://doi.org/10.1088/1361-6471/aaa2bf>
15. A. Obertelli, Nuclear structure from direct reactions with rare isotopes: observables, methods and highlights. Eur. Phys. J. Plus **131**, 319 (2016). <https://doi.org/10.1140/epjp/i2016-16319-8>
16. B.P. Kay, J.P. Schiffer, S.J. Freeman, Quenching of cross sections in nucleon transfer reactions. Phys. Rev. Lett. **111**, 042502 (2013). <https://doi.org/10.1103/PhysRevLett.111.042502>
17. W.N. Catford, What can we learn from transfer, and how is best to do it?, in The Euroschool on Exotic Beams, Vol. IV, Chapter 3 (2014). https://doi.org/10.1007/978-3-642-45141-6_3
18. I.J. Thompson, Coupled reaction channels calculations in nuclear physics. Comput. Phys. Rep. **7**, 167–212 (1988). [https://doi.org/10.1016/0167-7977\(88\)90005-6](https://doi.org/10.1016/0167-7977(88)90005-6)
19. W.W. Daehnick, J.D. Childs, Z. Vrcelj, Global optical model potential for elastic deuteron scattering from 12 to 90 MeV. Phys. Rev. C **21**, 2253 (1980). <https://doi.org/10.1103/PhysRevC.21.2253>

20. A.J. Koning, J.P. Delaroche, Local and global nucleon optical models from 1 keV to 200 MeV. *Nucl. Phys. A* **713**, 231–310 (2003). [https://doi.org/10.1016/S0375-9474\(02\)01321-0](https://doi.org/10.1016/S0375-9474(02)01321-0)
21. DWUCK. <https://www.oecd-nea.org/tools/abstract/detail/nesc9872>. Accessed 9 Dec 2019
22. R.C. Johnson, P.J.R. Soper, Contribution of deuteron breakup channels to deuteron stripping and elastic scattering. *Phys. Rev. C* **1**, 976 (1970). <https://doi.org/10.1103/PhysRevC.1.976>
23. R.C. Johnson, P.C. Tandy, An approximate three-body theory of deuteron stripping. *Nucl. Phys. A* **235**, 56–74 (1974). [https://doi.org/10.1016/0375-9474\(74\)90178-X](https://doi.org/10.1016/0375-9474(74)90178-X)
24. V.R. Pandharipande, I. Sick, P.K.A. de Witt Huberts, Independent particle motion and correlations in fermion systems. *Rev. Mod. Phys.* **69**, 981 (1997). <https://doi.org/10.1103/RevModPhys.69.981>
25. J.P. Schiffer, C.R. Hoffman, B.P. Kay et al., Test of sum rules in nucleon transfer reactions. *Phys. Rev. Lett.* **108**, 022501 (2012). <https://doi.org/10.1103/PhysRevLett.108.022501>
26. S.D. Pain, W.N. Catford, N.A. Orr et al., Structure of ^{12}Be : intruder d -wave strength at $N = 8$. *Phys. Rev. Lett.* **96**, 032502 (2006). <https://doi.org/10.1103/PhysRevLett.96.032502>
27. R. Kanungo, A.T. Gallant, M. Uchida et al., Structure of states in ^{12}Be via the $^{11}\text{Be}(d, p)$ reaction. *Phys. Lett. B* **682**, 391–395 (2010). <https://doi.org/10.1016/j.physletb.2009.11.025>
28. M.H. Macfarlane, J.B. French, Stripping reactions and the structure of light and intermediate nuclei. *Rev. Mod. Phys.* **32**, 567 (1960). <https://doi.org/10.1103/RevModPhys.32.567>
29. A.H. Wuosmaa, B.B. Back, S. Baker et al., $^{15}\text{C}(d, p)^{16}\text{C}$ reaction and exotic behavior in ^{16}C . *Phys. Rev. Lett.* **105**, 132501 (2010). <https://doi.org/10.1103/PhysRevLett.105.132501>
30. S. Bedoor, A.H. Wuosmaa, J.C. Lighthall et al., Structure of ^{14}B and the evolution of $N = 9$ single-neutron isotones. *Phys. Rev. C* **88**, 011304(R) (2013). <https://doi.org/10.1103/PhysRevC.88.011304>
31. C.R. Hoffman, B.B. Back, B.P. Kay et al., Experimental study of the $^{19}\text{O}(d, p)^{20}\text{O}$ reaction in inverse kinematics. *Phys. Rev. C* **85**, 054318 (2012). <https://doi.org/10.1103/PhysRevC.85.054318>
32. J. Chen, K. Auranen, M.L. Avila et al., Experimental study of the low-lying negative-parity states in ^{11}Be using the $^{12}\text{B}(d, ^3\text{He})^{11}\text{Be}$ reaction. *Phys. Rev. C* **100**, 064314 (2019). <https://doi.org/10.1103/PhysRevC.100.064314>
33. M. Baranger, A definition of the single-nucleon potential. *Nucl. Phys. A* **149**, 225–240 (1970). [https://doi.org/10.1016/0375-9474\(70\)90692-5](https://doi.org/10.1016/0375-9474(70)90692-5)
34. R.J. Peterson, H.C. Bhang, J.J. Hamill et al., The $^{14}\text{C}(\alpha, \alpha')^{14}\text{C}$ and $^{13}\text{C}(d, p)^{14}\text{C}$ reactions. *Nucl. Phys. A* **425**, 469–492 (1984). [https://doi.org/10.1016/0375-9474\(84\)90020-4](https://doi.org/10.1016/0375-9474(84)90020-4)
35. S. Agostinelli, J. Allison, K. Amako et al., Geant4—a simulation toolkit. *Nucl. Instrum. Methods Phys. Res. A* **506**, 250–303 (2003). [https://doi.org/10.1016/S0168-9002\(03\)01368-8](https://doi.org/10.1016/S0168-9002(03)01368-8)
36. E. Pollacco, D. Beaumel, P. Roussel-Chomaz et al., MUST2: a new generation array for direct reaction studies. *Eur. Phys. J. A* **25**(s01), 287–288 (2005). <https://doi.org/10.1140/epjad/i2005-06-162-5>
37. M. Labiche, W.N. Catford, R.C. Lemmon et al., TIARA: a large solid angle silicon array for direct reaction studies with radioactive beams. *Nucl. Instrum. Methods Phys. Res. A* **614**, 439–448 (2010). <https://doi.org/10.1016/j.nima.2010.01.009>
38. MUST2 website. <http://must2.cea.fr/index.php?id=5&ref=1>. Accessed 14 Nov 2019
39. T. Al Kalanee, J. Gibelin, P. Roussel-Chomaz et al., Structure of unbound neutron-rich ^9He studied using single-neutron transfer. *Phys. Rev. C* **88**, 034301 (2013). <https://doi.org/10.1103/PhysRevC.88.034301>
40. A. Matta, D. Beaumel, H. Otsu et al., New findings on structure and production of ^{10}He from ^{11}Li with the $(d, ^3\text{He})$ reaction. *Phys. Rev. C* **92**, 041302(R) (2015). <https://doi.org/10.1103/PhysRevC.92.041302>
41. F. Flavigny, A. Gillibert, L. Nalpas et al., Limited asymmetry dependence of correlations from single nucleon transfer. *Phys. Rev. Lett.* **110**, 122503 (2013). <https://doi.org/10.1103/PhysRevLett.110.122503>
42. B. Fernandez-Dominguez, J.S. Thomas, W.N. Catford et al., Emergence of the $N=16$ shell gap in ^{21}O . *Phys. Rev. C* **84**, 011301(R) (2011). <https://doi.org/10.1103/PhysRevC.84.011301>
43. S. Giron, F. Hammache, N. de Séréville et al., Spectroscopy of ^{61}Fe via the neutron transfer reaction $^2\text{H}(^{60}\text{Fe}, p)^{61}\text{Fe}^*$. *Phys. Rev. C* **95**, 035806 (2017). <https://doi.org/10.1103/PhysRevC.95.035806>
44. G. Burgunder, O. Sorlin, F. Nowacki et al., Experimental study of the two-body spin-orbit force in nuclei. *Phys. Rev. Lett.* **112**, 042502 (2014). <https://doi.org/10.1103/PhysRevLett.112.042502>
45. J. Diriken, N. Patronis, A.N. Andreyev et al., Study of the deformation-driving $\nu d_{5/2}$ orbital in $^{67}\text{Ni}_{39}$ using one-neutron transfer reactions. *Phys. Lett. B* **736**, 533–538 (2014). <https://doi.org/10.1016/j.physletb.2014.08.004>
46. W.N. Catford, C.N. Timis, R.C. Lemmon et al., Migration of nuclear shell gaps studied in the $d(^{24}\text{Ne}, p\gamma)^{24}\text{Ne}$ reaction. *Phys. Rev. Lett.* **104**, 192501 (2010). <https://doi.org/10.1103/PhysRevLett.104.192501>
47. F. Delaunay, B. Fernández-Domínguez, N.L. Achouri, et al., Single-particle structure of ^{17}C studied with the $^{16}\text{C}(d, p)$ transfer reaction, in 20th Colloque GANIL, Amboise, 15–17 Oct 2017 (2017)
48. Th Kroll, V. Bildstein, K. Wimmer et al., Transfer reactions on neutron-rich nuclei at REX-ISOLDE. *AIP Conf. Proc.* **1165**, 363 (2009). <https://doi.org/10.1063/1.3232117>
49. R. Orlandi, D. Mucher, R. Raabe et al., Single-neutron orbits near ^{78}Ni : spectroscopy of the $N = 49$ isotope ^{79}Zn . *Phys. Lett. B* **740**, 298–302 (2015). <https://doi.org/10.1016/j.physletb.2014.12.006>
50. V. Bildstein, R. Gernhäuser, T. Kröll et al., T-REX: a new setup for transfer experiments at REX-ISOLDE. *Eur. Phys. J. A* **48**, 85 (2012). <https://doi.org/10.1140/epja/i2012-12085-6>
51. J. Eberth, G. Pascovici, H.G. Thomas et al., MINIBALL A Ge detector array for radioactive ion beam facilities. *Prog. Part. Nucl. Phys.* **46**, 389–398 (2001). [https://doi.org/10.1016/S0146-6410\(01\)00145-4](https://doi.org/10.1016/S0146-6410(01)00145-4)
52. N. Warr, J. Van de Walle, M. Albers et al., The miniball spectrometer. *Eur. Phys. J. A* **49**, 40 (2013). <https://doi.org/10.1140/epja/i2013-13040-9>
53. S.D. Pain, J.A. Cizewski, R. Hatarik et al., Development of a high solid-angle silicon detector array for measurement of transfer reactions in inverse kinematics. *Nucl. Instrum. Methods Phys. Res. B* **261**, 11223–1125 (2007). <https://doi.org/10.1016/j.nimb.2007.04.289>
54. D.W. Bardayan, S. Ahn, J.C. Blackmon et al., Construction and commissioning of the SuperORRUBA detector. *Nucl. Instrum. Methods Phys. Res. A* **711**, 160–165 (1999). <https://doi.org/10.1016/j.nima.2013.01.035>
55. J. Belarge, S.A. Kuvin, L.T. Baby et al., Experimental investigation of the $^{19}\text{Ne}(p, \gamma)^{20}\text{Na}$ reaction rate and implications for breakout from the hot CNO cycle. *Phys. Rev. Lett.* **117**, 182701 (2016). <https://doi.org/10.1103/PhysRevLett.117.182701>
56. K.T. Schmitt, K.L. Jones, S. Ahn et al., Reactions of a ^{10}Be beam on proton and deuteron targets. *Phys. Rev. C* **88**, 064612 (2013). <https://doi.org/10.1103/PhysRevC.88.064612>

57. I-Yang LEE, The GAMMASPHERE. Nucl. Phys. A **520**, c641–c655 (1990). [https://doi.org/10.1016/0375-9474\(90\)91181-P](https://doi.org/10.1016/0375-9474(90)91181-P)
58. S. Paschalis, I.Y. Lee, A.O. Macchiavelli et al., The performance of the gamma-ray energy tracking in-beam nuclear array GRETINA. Nucl. Instrum. Methods Phys. Res. A **709**, 44–55 (2013). <https://doi.org/10.1016/j.nima.2013.01.009>
59. M.S. Wallace, M.A. Famiano, M.-J. van Goethem et al., The high resolution array (HiRA) for rare isotope beam experiments. Nucl. Instrum. Methods Phys. Res. A **583**, 302–312 (2007). <https://doi.org/10.1016/j.nima.2007.08.248>
60. B. Davin, R.T. de Souza, R. Yanez et al., LASSA: a large area silicon strip array for isotopic identification of charged particles. Nucl. Instrum. Methods Phys. Res. A **473**, 302–318 (2001). [https://doi.org/10.1016/S0168-9002\(01\)00295-9](https://doi.org/10.1016/S0168-9002(01)00295-9)
61. J. Lee, M.B. Tsang, D. Bazin et al., Neutron-proton asymmetry dependence of spectroscopic factors in Ar isotopes. Phys. Rev. Lett. **104**, 112701 (2010). <https://doi.org/10.1103/PhysRevLett.104.112701>
62. A. Sanetullaev, M.B. Tsang, W.G. Lynch et al., Neutron spectroscopic factors of ^{55}Ni hole-states from (p , d)transfer reactions. Phys. Lett. B **736**, 137–141 (2014). <https://doi.org/10.1016/j.physletb.2014.07.003>
63. C.Aa Diget, S.P. Fox, A. Smith et al., SHARC: silicon highly-segmented array for reactions and coulex used in conjunction with the TIGRESS γ -ray spectrometer. J. Instrum. **6**, P02005 (2011). <https://doi.org/10.1088/1748-0221/6/02/P02005>
64. M.A. Schumaker, G. Hackman, C.J. Pearson et al., Measured and simulated performance of Compton-suppressed TIGRESS HPGe clover detectors. Nucl. Instrum. Methods Phys. Res. A **570**, 437–445 (2007). <https://doi.org/10.1016/j.nima.2006.10.185>
65. R. Kanungo, IRIS: the ISAC charged particle reaction spectroscopy facility for reaccelerated high-energy ISOL beams. Hyperfine Interact **225**, 235–240 (2015). <https://doi.org/10.1007/s10751-013-0904-8>
66. J. Manfredi, J. Lee, W.G. Lynch et al., On determining dead layer and detector thicknesses for a position-sensitive silicon detector. Nucl. Instrum. Methods Phys. Res. A **888**, 177–183 (2018). <https://doi.org/10.1016/j.nima.2017.12.082>
67. Z. Elekes, Zs Dombrádi, N. Aoi, Spectroscopic study of neutron shell closures via nucleon transfer in the near-dripline nucleus ^{23}O . Phys. Rev. Lett. **98**, 102502 (2007). <https://doi.org/10.1103/PhysRevLett.98.102502>
68. Z. Elekes, Zs Dombrádi, N. Aoi et al., Search for neutron decoupling in ^{22}O via the (d , $d'\gamma$) reaction. Phys. Rev. C **74**, 017306 (2006). <https://doi.org/10.1103/PhysRevC.74.017306>
69. S. Takeuchi, T. Motobayashi, Y. Togano et al., DALI2: a NaI(Tl) detector array for measurements of γ rays from fast nuclei. Nucl. Instrum. Methods Phys. Res. A **763**, 596–603 (2014). <https://doi.org/10.1016/j.nima.2014.06.087>
70. T. Shimoda, H. Miyatake, S. Morinobu, Design study of the secondary-beam line at RCNP. Nucl. Instrum. Methods Phys. Res. Sect. B **70**, 320–330 (1992). [https://doi.org/10.1016/0168-583X\(92\)95948-Q](https://doi.org/10.1016/0168-583X(92)95948-Q)
71. S. Beceiro-Novo, T. Ahn, D. Bazin et al., Active targets for the study of nuclei far from stability. Prog. Part. Nucl. Phys. **84**, 124–165 (2015). <https://doi.org/10.1016/j.pnpnp.2015.06.003>
72. C.E. Demonchy, M. Caamano, H. Wang et al., MAYA: an active-target detector for binary reactions with exotic. Nucl. Instrum. Methods Phys. Res. A **583**, 341–349 (2007). <https://doi.org/10.1016/j.nima.2007.09.022>
73. C. Monrozeau, E. Khan, Y. Blumenfeld et al., First measurement of the giant monopole and quadrupole resonances in a short-lived nucleus: ^{56}Ni . Phys. Rev. Lett. **100**, 042501 (2008). <https://doi.org/10.1103/PhysRevLett.100.042501>
74. S. Bagchi, J. Gibelin, M.N. Harakeh et al., Observation of isoscalar multipole strengths in exotic doubly-magic ^{56}Ni in inelastic α scattering in inverse kinematics. Phys. Lett. B **751**, 371–375 (2015). <https://doi.org/10.1016/j.physletb.2015.10.060>
75. M. Vandebrouck, J. Gibelin, E. Khan et al., Measurement of the isoscalar monopole response in the neutron-rich nucleus ^{68}Ni . Phys. Rev. Lett. **113**, 032504 (2014). <https://doi.org/10.1103/PhysRevLett.113.032504>
76. M. Vandebrouck, J. Gibelin, E. Khan et al., Isoscalar response of ^{68}Ni to α -particle and deuteron probes. Phys. Rev. C **92**, 024316 (2015). <https://doi.org/10.1103/PhysRevC.92.024316>
77. J. Giovinazzo, J. Pibernat, T. Goigoux et al., Metal-core pad-plane development for ACTAR TPC. Nucl. Instrum. Methods Phys. Res. A **892**, 114–121 (2018). <https://doi.org/10.1016/j.nima.2018.03.007>
78. B. Mauss, P. Morfouace, T. Roger et al., Commissioning of the Active TARget and time projection chamber (ACTAR TPC). Nucl. Instrum. Methods Phys. Res. A **940**, 498–504 (2019). <https://doi.org/10.1016/j.nima.2019.06.067>
79. D. Bazin, J. Bradt, Y. Ayyad et al., The active target time projection chamber at NSCL. EPJ Web Conf. **163**, 00004 (2017). <https://doi.org/10.1051/epjconf/201716300004>
80. J. Bradt, D. Bazin, F. Abu-Nimeh et al., Commissioning of the active-target time projection chamber. Nuclear Instrum. Methods Phys. Res. A **875**, 65–79 (2017). <https://doi.org/10.1016/j.nima.2017.09.013>
81. D. Suzuki, M. Ford, D. Bazin et al., Prototype AT-TPC: toward a new generation active target time projection chamber for radioactive beam experiments. Nucl. Instrum. Methods Phys. Res. A **691**, 39–54 (2012). <https://doi.org/10.1016/j.nima.2012.06.050>
82. T. Furuno, T. Kawabata, H.J. Ong et al., Performance test of the MAIKo active target. Nucl. Instrum. Methods Phys. Res. A **908**, 215–224 (2018). <https://doi.org/10.1016/j.nima.2018.08.042>
83. T. Furuno, T. Kawabata, S. Adachi et al., Signature of $Z = 6$ subshell closure in ^{10}C from the $^{10}\text{C}(\alpha, \alpha')$ measurement with the MAIKo active target. Phys. Rev. C **100**, 054322 (2019). <https://doi.org/10.1103/PhysRevC.100.054322>
84. J.Y. Xu, Q.T. Li, Y.L. Ye et al., Performance of a small AT-TPC prototype. Nucl. Sci. Tech. **29**, 97 (2018). <https://doi.org/10.1007/s41365-018-0437-6>
85. W. Huang, F. Lu, H. Li et al., Laser test of the prototype of CEE time projection chamber. Nucl. Sci. Tech. **29**, 41 (2018). <https://doi.org/10.1007/s41365-018-0382-4>
86. A.H. Wuosmaa, J.P. Schiffer, B.B. Back et al., A solenoidal spectrometer for reactions in inverse kinematics. Nucl. Instrum. Methods Phys. Res. A **580**, 1290–1300 (2007). <https://doi.org/10.1016/j.nima.2007.07.029>
87. A.H. Wuosmaa, T. Al Tahtamouni, J.P. Schiffer et al., A solenoidal transport device for transfer reactions in inverse kinematics. Nucl. Phys. A **746**, 267c–271c (2004). <https://doi.org/10.1016/j.nuclphysa.2004.09.039>
88. D. Santiago-Gonzalez, K. Auranen, M.L. Avila et al., Probing the single-particle character of rotational states in ^{19}F using a short-lived isomeric beam. Phys. Rev. Lett. **120**, 122503 (2014). <https://doi.org/10.1103/PhysRevLett.120.122503>
89. S. Almaraz-Calderon, K.E. Rehm, N. Gerken et al., Study of the $^{26}\text{Al}^m(d, p)^{27}\text{Al}$ reaction and the influence of the $^{26}\text{Al}^{10+}$ isomer on the destruction of ^{26}Al in the galaxy. Phys. Rev. Lett. **119**, 072701 (2014). <https://doi.org/10.1103/PhysRevLett.119.072701>
90. B.B. Back, S.I. Baker, B.A. Brown et al., First experiment with HELIOS: the structure of ^{13}B . Phys. Rev. Lett. **104**, 132501 (2010). <https://doi.org/10.1103/PhysRevLett.104.132501>

91. I. Tanihata, H. Hamagaki, O. Hashimoto et al., Measurements of interaction cross sections and nuclear radii in the light p -shell region. *Phys. Rev. Lett.* **55**, 2676 (1985). <https://doi.org/10.1103/PhysRevLett.55.2676>
92. D. Bazin, W. Benenson, B.A. Brown et al., Probing the halo structure of $^{19,17,15}\text{C}$ and ^{14}B . *Phys. Rev. C* **57**, 2156 (1998). <https://doi.org/10.1103/PhysRevC.57.2156>
93. E. Sauvan, F. Carstoiu, N.A. Orr et al., One-neutron removal reactions on light neutron-rich nuclei. *Phys. Rev. C* **69**, 044603 (2004). <https://doi.org/10.1103/PhysRevC.69.044603>
94. V. Guimarães, J.J. Kolata, D. Bazin et al., Spectroscopy of $^{13,14}\text{B}$ via the one-neutron knockout reaction. *Phys. Rev. C* **61**, 064609 (2000). <https://doi.org/10.1103/PhysRevC.61.064609>
95. S. Bedoor, A.H. Wuosmaa, M. Albers et al., Structure of ^{14}C and ^{14}B from the $^{14,15}\text{C}(d, ^3\text{He})^{13,14}\text{B}$ reactions. *Phys. Rev. C* **93**, 044323 (2016). <https://doi.org/10.1103/PhysRevC.93.044323>
96. M. Labiche, N.A. Orr, F.M. Marqués et al., Halo structure of ^{14}Be . *Phys. Rev. Lett.* **86**, 600 (2001). <https://doi.org/10.1103/PhysRevLett.86.600>
97. T. Kobayashi, O. Yamakawa, K. Omata et al., Projectile fragmentation of the extremely neutron-rich nucleus ^{11}Li at 0.79 GeV/nucleon. *Phys. Rev. Lett.* **60**, 2599 (1988). <https://doi.org/10.1103/PhysRevLett.60.2599>
98. T. Myo, K. Kato, H. Toki et al., Roles of tensor and pairing correlations on halo formation in ^{11}Li . *Phys. Rev. C* **76**, 024305 (2007). <https://doi.org/10.1103/PhysRevC.76.024305>
99. I. Tanihata, M. Alcorta, D. Bandyopadhyay et al., Measurement of the two-halo neutron transfer reaction $^1\text{H}(^{11}\text{Li}, ^9\text{Li})^3\text{H}$ at 3A MeV. *Phys. Rev. Lett.* **100**, 192502 (2008). <https://doi.org/10.1103/PhysRevLett.100.192502>
100. H.Y. Lee, J.P. Greene, C.L. Jiang et al., Experimental study of the $^{11,12}\text{B}(n, \gamma)$ reactions and their influence on r -process nucleosynthesis of light elements. *Phys. Rev. C* **81**, 015802 (2010). <https://doi.org/10.1103/PhysRevC.81.015802>
101. J.S. Winfield, S. Fortier, W.N. Catford et al., Structure of Be^{11} from the (p, d) reaction in inverse kinematics. *J. Phys. G Nucl. Part. Phys.* **25**, 755–757 (1999). <https://doi.org/10.1088/0954-3899/25/4/029>
102. A. Lemasson, A. Navin, N. Keeley et al., Reactions with the double-Borromean nucleus ^8He . *Phys. Rev. C* **82**, 044617 (2010). <https://doi.org/10.1103/PhysRevC.82.044617>
103. N. Keeley, F. Skaza, V. Lapoux et al., Probing the ^8He ground state via the $^8\text{He}(p, t)^6\text{He}$ reaction. *Phys. Lett. B* **646**, 222–226 (2007). <https://doi.org/10.1016/j.physletb.2007.01.035>
104. P. Mueller, I.A. Sulai, A.C.C. Villari et al., Nuclear charge radius of ^8He . *Phys. Rev. Lett.* **99**, 252501 (2007). <https://doi.org/10.1103/PhysRevLett.99.252501>
105. A. Lemasson, A. Shrivastava, A. Navin et al., Modern rutherford experiment: tunneling of the most neutron-rich nucleus. *Phys. Rev. Lett.* **103**, 232701 (2009). <https://doi.org/10.1103/PhysRevLett.103.232701>
106. A. Lemasson, A. Navin, M. Rejmund et al., Pair and single neutron transfer with Borromean ^8He . *Phys. Lett. B* **697**, 454–458 (2011). <https://doi.org/10.1016/j.physletb.2011.02.038>
107. M.V. Zhukov, A.A. Korshennikov, M.H. Smedberg, Simplified $\alpha + 4n$ model for the ^8He nucleus. *Phys. Rev. C* **50**, R1(R) (1994). <https://doi.org/10.1103/PhysRevC.50.R1>
108. K. Hagino, N. Takahashi, H. Sagawa, Strong dineutron correlation in ^8He and ^{18}C . *Phys. Rev. C* **77**, 054317 (2008). <https://doi.org/10.1103/PhysRevC.77.054317>
109. Y. Kanada-En'yo, Dineutron structure in ^8He . *Phys. Rev. C* **76**, 044323 (2007). <https://doi.org/10.1103/PhysRevC.76.044323>
110. S. Aoyama, N. Itagaki, M. Oi, Systematic analyses of the $t + t$ clustering effect in He isotopes. *Phys. Rev. C* **74**, 017307 (2006). <https://doi.org/10.1103/PhysRevC.74.017307>
111. N. Itagaki, M. Ito, K. Arai et al., Mixing of di-neutron components in ^8He . *Phys. Rev. C* **78**, 017306 (2008). <https://doi.org/10.1103/PhysRevC.78.017306>
112. R. Wolski et al., in *Clustering Aspects of Quantum Many-Body Systems*, ed. by A. Ohnishi, N. Itagaki, Y. Kanada-Enyo, K. Kato (World Scientific, Singapore, 2001), p. 15. <https://doi.org/10.1142/4946>
113. A.A. Korshennikov, EYu. Nikolskii, E.A. Kuzmin et al., Experimental evidence for the existence of ^7H and for a specific structure of ^8He . *Phys. Rev. Lett.* **90**, 082501 (2003). <https://doi.org/10.1103/PhysRevLett.90.082501>
114. A.A. Korshennikov, M.S. Golovkov, I. Tanihata et al., Superheavy hydrogen ^5H . *Phys. Rev. Lett.* **87**, 092501 (2001). <https://doi.org/10.1103/PhysRevLett.87.092501>
115. K.L. Jones, Transfer reaction experiments with radioactive beams: from halos to the r -process. *Phys. Scr.* **T152**, 014020 (2013). <https://doi.org/10.1088/0031-8949/2013/T152/014020>
116. A.A. Korshennikov, M.S. Golovkov, A. Ozawa et al., Observation of an excited state in ^7He with unusual structure. *Phys. Rev. Lett.* **82**, 3581 (1999). <https://doi.org/10.1103/PhysRevLett.82.3581>
117. K. Hagino, H. Sagawa, T. Nakamura et al., Two-particle correlations in continuum dipole transitions in Borromean nuclei. *Phys. Rev. C* **80**, 031301(R) (2009). <https://doi.org/10.1103/PhysRevC.80.031301>
118. F. Skaza, V. Lapoux, N. Keeley et al., Experimental evidence for subshell closure in ^8He and indication of a resonant state in ^7He below 1 MeV. *Phys. Rev. C* **73**, 044301 (2006). <https://doi.org/10.1103/PhysRevC.73.044301>
119. M. Vorabbi, A. Calci, P. Navrátil et al., Structure of the exotic ^9He nucleus from the no-core shell model with continuum. *Phys. Rev. C* **97**, 034314 (2018). <https://doi.org/10.1103/PhysRevC.97.034314>
120. M.S. Golovkov, L.V. Grigorenko, A.S. Fomichev et al., New insight into the low-energy ^9He spectrum. *Phys. Rev. C* **76**, 021605(R) (2007). <https://doi.org/10.1103/PhysRevC.76.021605>
121. L. Chen, B. Blank, B.A. Brown et al., Evidence for an $l = 0$ ground state in ^9He . *Phys. Lett. B* **505**, 21–26 (2001). [https://doi.org/10.1016/S0370-2693\(01\)00313-6](https://doi.org/10.1016/S0370-2693(01)00313-6)
122. E. Garrido, D.V. Fedorov, A.S. Jensen, The ^{10}Li spectrum and the ^{11}Li properties. *Nucl. Phys. A* **700**, 117–141 (2002). [https://doi.org/10.1016/S0375-9474\(01\)01310-0](https://doi.org/10.1016/S0375-9474(01)01310-0)
123. H.B. Jeppesen, A.M. Moro, U.C. Bergmann et al., Study of ^{10}Li via the $^9\text{Li}(^2\text{H}, p)$ reaction at REX-ISOLDE. *Phys. Lett. B* **642**, 449–454 (2006). <https://doi.org/10.1016/j.physletb.2006.09.060>
124. P. Santi, J.J. Kolata, V. Guimarães et al., Structure of the ^{10}Li nucleus investigated via the $^9\text{Li}(d, p)^{10}\text{Li}$ reaction. *Phys. Rev. C* **67**, 024606 (2003). <https://doi.org/10.1103/PhysRevC.67.024606>
125. A.M. Moro, J. Casal, M. Gómez-Ramos, Investigating the ^{10}Li continuum through $^9\text{Li}(d, p)^{10}\text{Li}$ reactions. *Phys. Lett. B* **793**, 13–18 (2019). <https://doi.org/10.1016/j.physletb.2019.04.015>
126. M. Cavallaro, M. De Napoli, F. Cappuzzello et al., Investigation of the ^{10}Li shell inversion by neutron continuum transfer reaction. *Phys. Rev. Lett.* **118**, 012701 (2017). <https://doi.org/10.1103/PhysRevLett.118.012701>
127. A. Sanetullaev, R. Kanungo, J. Tanaka et al., Investigation of the role of ^{10}Li resonances in the halo structure of ^{11}Li through the $^{11}\text{Li}(p, d)^{10}\text{Li}$ transfer reaction. *Phys. Lett. B* **755**, 481–485 (2016). <https://doi.org/10.1016/j.physletb.2016.02.060>

128. J. Casal, M. Gómez-Ramos, A.M. Moro, Description of the $^{11}\text{Li}(p, d)^{10}\text{Li}$ transfer reaction using structure overlaps from a full three-body model. *Phys. Lett. B* **767**, 307–313 (2017). <https://doi.org/10.1016/j.physletb.2017.02.017>
129. D.H. Wilkinson, D.E. Alburger, Beta decay of Be^{11} . *Phys. Rev.* **113**, 563 (1959). <https://doi.org/10.1103/PhysRev.113.563>
130. I. Talmi, I. Unna, Order of levels in the shell model and spin of Be^{11} . *Phys. Rev. Lett.* **4**, 469 (1960). <https://doi.org/10.1103/PhysRevLett.4.469>
131. J.S. Winfield, S. Fortier, W.N. Catford et al., Single-neutron transfer from $^{11}\text{Be}_{\text{gs}}$ via the (p, d) reaction with a radioactive beam. *Nucl. Phys. A* **683**, 48–78 (2001). [https://doi.org/10.1016/S0375-9474\(00\)00463-2](https://doi.org/10.1016/S0375-9474(00)00463-2)
132. S. Fortier, S. Pita, J.S. Winfield et al., Core excitation in $^{11}\text{Be}_{\text{gs}}$ via the $p(^{11}\text{Be}, ^{10}\text{Be})d$. *Phys. Lett. B* **461**, 22–27 (1999). [https://doi.org/10.1016/S0370-2693\(99\)00825-4](https://doi.org/10.1016/S0370-2693(99)00825-4)
133. J. Ying, J.-L. Lou, Y.L. Ye et al., A new measurement of $^{11}\text{Be}(p, d)$ transfer reaction. *Chin. Phys. Lett.* **35**, 082501 (2018). <https://doi.org/10.1088/0256-307X/35/8/082501>
134. H.T. Fortune, R. Sherr, Consistent description of ^{11}Be and ^{12}Be and of the $^{11}\text{Be}(d, p)^{12}\text{Be}$ reaction. *Phys. Rev. C* **85**, 051303(R) (2012). <https://doi.org/10.1103/PhysRevC.85.051303>
135. J.G. Johansen, V. Bildstein, M.J.G. Borge et al., Experimental study of bound states in ^{12}Be through low-energy $^{11}\text{Be}(d, p)$ -transfer reactions. *Phys. Rev. C* **88**, 044619 (2013). <https://doi.org/10.1103/PhysRevC.88.044619>
136. J. Chen, J.L. Lou, Y.L. Ye et al., Low-lying states in ^{12}Be using one-neutron transfer reaction. *Phys. Rev. C* **98**, 014616 (2018). <https://doi.org/10.1103/PhysRevC.98.014616>
137. S. Ota, S. Shimoura, H. Iwasaki et al., Low-lying proton intruder state in ^{13}B . *Phys. Lett. B* **666**, 311–314 (2008). <https://doi.org/10.1016/j.physletb.2008.07.081>
138. H. Iwasaki, A. Dewald, C. Fransen et al., Low-lying neutron intruder state in ^{13}B and the fading of the $N = 8$ shell closure. *Phys. Rev. Lett.* **102**, 202502 (2009). <https://doi.org/10.1103/PhysRevLett.102.202502>
139. J.D. Goss, P.L. Jolivet, C.P. Browne et al., Angular distribution measurements for $^{14}\text{C}(d, p)^{15}\text{C}$ and the level structure of ^{15}C . *Phys. Rev. C* **12**, 1730 (1975). <https://doi.org/10.1103/PhysRevC.12.1730>
140. H.T. Fortune, Matter radii and configuration mixing in $^{15-19}\text{C}$. *Eur. Phys. J. A* **54**, 73 (2018). <https://doi.org/10.1140/epja/i2018-12506-6>
141. C.R. Hoffman, B.P. Kay, J.P. Schiffer et al., Neutron s states in loosely bound nuclei. *Phys. Rev. C* **89**, 061305(R) (2014). <https://doi.org/10.1103/PhysRevC.89.061305>
142. D.W. Bardayan, P.D. O'Malley, J.C. Blackmon et al., Spectroscopic study of low-lying ^{16}N levels. *Phys. Rev. C* **78**, 052801(R) (2008). <https://doi.org/10.1103/PhysRevC.78.052801>
143. T.L. Ma, B. Guo, Z.H. Li et al., Precision measurement of the angular distribution for the $^{16}\text{O}(d, p)^{17}\text{O}$ transfer reaction to the ground state of ^{17}O . *Nucl. Phys. A* **986**, 26–33 (2019). <https://doi.org/10.1016/j.nuclphysa.2019.03.004>
144. J. Chen, C.R. Hoffman, T. Ahn et al., Experimental study of the effective nucleon–nucleon interaction using the $^{21}\text{F}(d, p)^{22}\text{F}$ reaction. *Phys. Rev. C* **98**, 014325 (2018). <https://doi.org/10.1103/PhysRevC.98.014325>
145. S.M. Brown, W.N. Catford, J.S. Thomas et al., Low-lying neutron fp -shell intruder states in ^{27}Ne . *Phys. Rev. C* **85**, 011302(R) (2012). <https://doi.org/10.1103/PhysRevC.85.011302>
146. G.L. Wilson, W.N. Catford, N.A. Orr et al., Shell evolution approaching the $N = 20$ island of inversion: structure of ^{26}Na . *Phys. Lett. B* **759**, 417–423 (2016). <https://doi.org/10.1016/j.physletb.2016.05.093>
147. A. Matta, W.N. Catford, N.A. Orr et al., Shell evolution approaching the $N = 20$ island of inversion: structure of ^{29}Mg . *Phys. Rev. C* **99**, 044320 (2019). <https://doi.org/10.1103/PhysRevC.99.044320>
148. L. Gaudefroy, O. Sorlin, F. Nowacki et al., Structure of the $N = 27$ isotones derived from the $^{44}\text{Ar}(d, p)^{45}\text{Ar}$ reaction. *Phys. Rev. C* **78**, 034307 (2008). <https://doi.org/10.1103/PhysRevC.78.034307>
149. L. Gaudefroy, O. Sorlin, D. Beaumel et al., Reduction of the spin-orbit splittings at the $N = 28$ shell closure. *Phys. Rev. Lett.* **97**, 092501 (2006). <https://doi.org/10.1103/PhysRevLett.97.092501>
150. J. Diriken, N. Patronis, A. Andreyev et al., Experimental study of the $^{66}\text{Ni}(d, p)^{67}\text{Ni}$ one-neutron transfer reaction. *Phys. Rev. C* **91**, 054321 (2015). <https://doi.org/10.1103/PhysRevC.91.054321>
151. P. Morfouace, S. Franchoo, K. Sieja et al., Single-particle strength in neutron-rich ^{69}Cu from the $^{70}\text{Zn}(d, ^3\text{He})^{69}\text{Cu}$ proton pick-up reaction. *Phys. Rev. C* **93**, 064308 (2016). <https://doi.org/10.1103/PhysRevC.93.064308>
152. P. Morfouace, S. Franchoo, K. Sieja et al., Evolution of single-particle strength in neutron-rich ^{71}Cu . *Phys. Lett. B* **751**, 306–310 (2015). <https://doi.org/10.1016/j.physletb.2015.10.064>
153. J.S. Thomas, G. Arbanas, D.W. Bardayan et al., Single-neutron excitations in neutron-rich ^{83}Ge and ^{85}Se . *Phys. Rev. C* **76**, 044302 (2007). <https://doi.org/10.1103/PhysRevC.76.044302>
154. S. Cruz, P.C. Bender, R. Krucken et al., Shape coexistence and mixing of low-lying 0^+ states in ^{96}Sr . *Phys. Lett. B* **786**, 94–99 (2018). <https://doi.org/10.1016/j.physletb.2018.09.031>
155. S. Cruz, K. Wimmer, P.C. Bender et al., Single-particle structure of neutron-rich Sr isotopes via $^2\text{H}(^{94,95,96}\text{Sr}, p)$ reactions. *Phys. Rev. C* **100**, 054321 (2019). <https://doi.org/10.1103/PhysRevC.100.054321>
156. K.L. Jones, A.S. Adekola, D.W. Bardayan et al., The magic nature of ^{132}Sn explored through the single-particle states of ^{133}Sn . *Nature* **465**, 454–457 (2010). <https://doi.org/10.1038/nature09048>
157. R. Orlandi, S.D. Pain, S. Ahn et al., Neutron-hole states in ^{131}Sn and spin-orbit splitting in neutron-rich nuclei. *Phys. Lett. B* **785**, 615–620 (2018). <https://doi.org/10.1016/j.physletb.2018.08.005>
158. T.J. Ross, R.O. Hughes, J.M. Allmond et al., Spectroscopy of ^{153}Gd and ^{157}Gd using the $(p, d\gamma)$ reaction. *Phys. Rev. C* **90**, 044323 (2014). <https://doi.org/10.1103/PhysRevC.90.044323>
159. Y.P. Xu, D.Y. Pang, X.Y. Yun et al., Proton-neutron asymmetry independence of reduced single-particle strengths derived from (p, d) reactions. *Phys. Lett. B* **790**, 308 (2019). <https://doi.org/10.1016/j.physletb.2019.01.034>
160. D.W. Bardayan, Transfer reaction in nuclear astrophysics. *J. Phys. G Nucl. Part. Phys.* **43**, 043001 (2016). <https://doi.org/10.1088/0954-3899/43/4/043001>